Shock and detonation modeling with the Mie-Grüneisen equation of state

M. Arienti, E. Morano, J. E. Shepherd

Graduate Aeronautical Laboratories, MS 205-45,
California Institute of Technology,
Pasadena, CA 91125 USA

Graduate Aeronautical Laboratories Report FM99-8
Revised version of draft 1999 report entitled "Nonreactive Euler Flows with Mie-Grüneisen equation of state for High Explosives".

April 22, 2004

Abstract

We consider the numerical simulation of inviscid reactive flows with application to high density explosive detonation. The numerical model is based on the Euler equations and the Mie-Grüneisen equation of state extended to treat chemical energy release and expanded states. The equations are computed with a Roe-Glaister solver on a Cartesian mesh. We present results for two substances, a binder and an explosive. Our solution method is verified against the exact solution of the shock tube problem for solid materials. We show under what conditions a "physical" expansion shock can appear in this example. We then address the problem of modeling expanded states, and show results for a two-dimensional shock diffraction around a sharp corner. In the last part of the paper, we introduce a detonation model that extends the Mie-Grüneisen equation of state to enable high explosive simulations without the complexity of mixture equations of state. We conclude with two examples of corner-turning computations carried out with a pressure-dependent reaction rate law.

Contents

List of Figures

List of Tables

1 Introduction

Numerical simulations of explosives must include the capability to reproduce the essential features of unsteady compressible flow, an equation of state for reactants and products, and a model of the chemical reaction processes. For gases, there are widely accepted models and approximations for equation of state, reaction rates, and reaction mechanisms. For example, many mathematical and analytical studies use the perfect gas equation with a constant energy release parameter and a single-step irreversible reaction. For solids, there are many models for both equation of state and reaction rate and no simple standard approach. The available models are essentially empirical in nature, although there have been intensive efforts to provide sound foundations based on statistical and quantum mechanics.

There are many issues in high explosive modeling: natural microstructure, reaction mechanisms, and equations of state are among the most important. In the present paper, we seek to examine only one issue - the construction of a simple equation of state that can be used to test numerical solution methods. The purpose of our modeling approach is not to offer more accurate engineering solutions to explosive simulations, but rather to provide the simplest possible model that retains the essential features of a high explosive equation of state. With this motivation in mind, after reviewing in Section 2 some of the previous work on numerical simulations of gaseous and solid explosives, in Section 3 we introduce the Mie-Grüneisen equation of state and provide formulas for the isentropic pressure, the sound speed, and the fundamental derivative of the material. Available numerical techniques based on the control volume approach are discussed in Section 4. In Section 5, we describe an algorithm to compute exactly the shock tube problem and we evaluate the performance of a Roe-Glaister solver. In Section 6, we present two-dimensional results of shock diffraction in a solid material. Finally, in Section 7, we include chemical energy release in the model and test the modified Roe-Glaister solver in the case of a detonation wave diffracting around a sharp corner.

2 Issues in numerical modeling of detonations

Detonations are supersonic combustion waves with a leading shock front. The shock wave ignites the reactive material while the volume expansion due to energy release pushes the shock into fresh reactants.

The shock wave in homogeneous materials is very thin, a few mean free paths in gases or a few molecules wide in homogeneous condensed explosives. The shock wave is thickened in heterogeneous material due to scattering at grain boundaries. The overall chemical reaction zone can be micrometers to millimeters in length depending on the specific composition of the reactants.

In this section, we give a brief overview of the present state of thermodynamic and reaction rate models for numerical simulation of detonations in gaseous and condensed explosives. We focus on fully developed detonations; detonation initiation is an important but much more difficult problem.

2.1 Gaseous detonation

For explosives in the gaseous state, the perfect gas equation of state has been extensively used in detonation simulations [36, 37]. Detailed and realistic chemical reaction mechanisms have become available for many hydrocarbon species, and it is a relatively simple matter to implement quantitatively accurate equations of state for both reactants and products by using the extensive database of thermochemical properties that has been built up by the combustion community over the last five decades [25, 31, 59].

Despite the availability of detailed reaction mechanisms for many fuel-oxidizer systems, many one-dimensional simulations and almost all multi-dimensional simulations in gases have used approximate thermochemical models because of computational restrictions. Only recently [38] have two-dimensional gaseous detonation simulations been carried out with the simplest (hydrogen-oxygen) detailed reaction mechanism. Reaction mechanism reduction, where the reaction network is reduced to a manageable number of relations between chemical species, is just beginning to be applied to detonation in gases – one of the first efforts was an application to the Zeldovich-von Neumann-Doering (ZND) structure [39]. Recently, a two-dimensional cellular structure computation by Oran [38] was successfully replicated with a reduced chemical mechanism [9].

2.2 Solid and liquid explosives

Detonation modeling of high explosives offers additional challenges. Reactions occur under extreme thermodynamic conditions, with pressures up to 60 GPa and temperatures up to 4000 K. While many equations of state under these conditions have been proposed, none is as reliable or simple to use as the perfect gas model. In addition, the development of reaction mechanisms for nitramine explosives, such as RDX and HMX, have lagged behind hydrocarbon fuel oxidation mechanisms. Those reaction mechanisms that have been developed are complex, involving up to 500 chemical reactions between almost 100 species, and are appropriate for low-pressure gaseous reactions only [3, 40]. There is no consensus about how the mechanism and rates will be affected by the dense surrounding medium. Finally, many solid explosives are not homogeneous and the reaction process is expected to be dominated by the presence of hot-spots, regions of intense reaction created at voids, grain boundaries, and defects [15].

These factors make the modeling of chemical reaction processes in high explosives an extremely challenging task. Combined with the additional complexity of the material microstructure in many high explosives, the situation has made it completely impractical to apply detailed reaction mechanisms. As a consequence, code implementation has been dominated by empirical models that specify how the reactants are depleted through an ad hoc reaction rate expression that is calibrated against experiments, such as the cylinder test [23] and shock initiation experiments. The empirical models are essentially blending algorithms that specify how the equation of state is represented in the reaction zone region and how rapidly the transition occurs between reactants and products. A recent study on detonation in TNT nicely illustrates this approach [26].

There are two general classes of reactive flow models: 1) Two-phase models which treat gases and solids separately, and 2) single-phase models that treat the mixture of reactants

and products as a single fluid with some effective mixture properties. The two-phase flow approach is exemplified by the work of Baer and Nunziato [1], where mixture theory is used to derive a set of coupled evolution equations that determine how the properties of each phase individually evolve. The solid and gas phases are not required to be in equilibrium since the equation of state for each phase is treated individually. Baer and Nunziato used a Helmoltz free-energy equation of state due to Hayes for the unreacted solid explosive, and the Jones-Wilkins-Lee (JWL) equation of state for the gaseous products. A number of issues arise in formulating [2] and solving [19] the model equation set. Despite this, the two-phase model has attracted a lot of attention for deflagration to detonation transition in which the explosive event begins with low-speed combustion.

The single-phase models are simpler and represent much of the engineering approach to modeling high explosives. Two models of this type are presented by Lee and Tarver [27] and Johnson et al. [24]. The common idea is to treat the mixture of detonation reactants and products as a single fluid with properties that represent a weighted average between reactants and products. The advantage is the simplification of the numerical scheme, since the single-fluid Euler equations govern the flow evolution.

In the perfect gas case, there is always a single fluid (with the equation of state provided by the gas mixture equations) as long as local thermodynamic equilibrium throughout the reaction zone can be assumed. In dense explosives, the key issue is how to create an effective single-fluid equation of state when the thermodynamic properties of products and reactants are separately provided. Since four independent state variables exist (two for each state of the material) and only two mixture thermodynamic properties (energy and mass density) define the state of a portion of fluid, two additional relations are needed to describe the mixture properties.

One solution is to assume local mechanical and thermal equilibrium of the mixture components. This is the approach followed by Johnson et al. [24], who use the Mie-Grüneisen equation of state [29] for the reactants and a modified JWL equation of state for the products. The equilibrium condition is enforced at each grid point in the flow by numerical solution of the implicit equilibrium relations. Another solution, proposed by Lee and Tarver [27], is to require a local pressure equilibration without constraining the temperature. In [27], the JWL equation of state is used for reactants and products with different fitting parameters. Additional assumptions have to be made with this model to obtain closure. Stewart et al. [50] have explored the consequences for the reactant zone structure of making alternate closure assumptions. They compare the extremes of perfect thermal equilibrium to complete thermal isolation of products and reactants. They also examine a simple ad hoc assumption by assuming a fixed ratio of reactant-to-product specific volume. Simulations based on either equilibrium or adiabatic assumptions show that this parameter varies over a relatively modest range. This work was based on the equations of state by Davis for both products [5] and reactants [6]. Stewart et al. [49] applied this ad hoc closure rule to the computation of detonation shock dynamics relations. An alternative approach, where the interaction between different phases is first given by the solution of a set of Riemann problems and then averaged over each computational cell, is proposed by Chinnayya et al. [4].

A common issue for single- and two-phase models is the choice of a reaction rate expression. Most of these models use depletion laws with pressure- or temperature-dependent rates. Lee and Tarver [27] proposed an "initiation and growth" model with a single deple-

tion variable (the mass fraction of products) and two pressure-dependent terms (the first describing the initiation of the reaction through hot-spot generation, the second modeling the growth of the reaction away from these centers). The model of Johnson et al. [24] uses several depletion variables to represent the fraction of the material in the hot-spots, the main burn process and, possibly, slower processes associated with recombination or carbon condensation far behind the front. Chemical rates depend on temperature, pressure, and the previous history of the material.

In the present work, we have opted for the single-phase model to directly take advantage of recent developments in numerical schemes for solving Euler equations. We also avoid the complexity of imposing local pressure and temperature equilibrium by using the Mie-Grüneisen equation of state (with the addition of an energy release term) throughout the reaction zone. This formulation is explicit in pressure as a function of energy, density, and mass fraction to avoid point implicit computations that more complex formulations require.

The reaction rate is a simple single-step pressure-dependent depletion law with fractional order. The absence of the Arrhenius term eliminates the need to compute the temperature of the mixture, while the fractional order of the depletion law results in a finite reaction zone length. At the end of the reaction of a Chapman-Jouguet (CJ) detonation wave, the particle velocity in the shock reference frame equals the local sound speed [14]. In this way, a finite reaction length minimizes the effect of disturbances created by rear boundary conditions.

3 Engineering model for high explosives

Plastic-bonded explosives are composed mainly of explosive with small amounts of elastomer binder. The explosive is a granulated material coated with the binder and pressed into the desired shape. In the present study, we have used solvent-pressed HMX (cyclotetramethylenetetranitramine), referred to as HMX_sp, as the model for our explosive, and polychlorotrifluoroethylene (Kel-F) as the model for a binder. Nominal values of the thermodynamic parameters which are used in the present computations were obtained from the literature [7] and are given in table 3.

Table 1: Thermodynamic parameters.

Substance	c_0 [km/s]	s	ρ_0 [g/cc]	$\mathcal{G}$
Kel-F	2.03	1.64	2.132	0.45
HMX_sp	3.07	1.79	1.891	0.70

3.1 Reactive Euler equations

The reactive multi-dimensional Euler equations are

$$\begin{cases} \dfrac{\partial \rho}{\partial t} + \nabla \cdot (\rho \mathbf{u}) = & 0 \\ \dfrac{\partial}{\partial t}(\lambda\,\rho) + \nabla \cdot (\lambda\,\rho \mathbf{u}) = & \rho\, R \\ \dfrac{\partial}{\partial t}(\rho \mathbf{u}) + \nabla \cdot (\rho \mathbf{u}\,\mathbf{u} + \mathbf{I} P) = & 0 \\ \dfrac{\partial}{\partial t}(\rho E) + \nabla \cdot \left[\rho \mathbf{u}\left(E + \dfrac{P}{\rho}\right)\right] = & 0, \end{cases} \tag{1}$$

where ρ is the density of the fluid, λ is the product mass fraction, R is the reaction rate, $\mathbf{u}$ is the velocity vector, P is the pressure, and e is the specific internal energy. $E = e + 1/2\,\|\mathbf{u}\|^2$ is the specific total energy. Throughout the paper, we will always refer to specific quantities, e.g. "energy" for "specific energy". Equation (1) may be rewritten in conservative form as

$$\mathbf{U}_t + \nabla \cdot \mathbf{F}(\mathbf{U}) = \mathbf{\Omega}(\mathbf{U}), \tag{2}$$

where $\mathbf{U} = (\rho, \lambda\,\rho, \rho\mathbf{u}, \rho E)^T$ is the vector of conservative variables.

The chemistry is based on a simple one-step irreversible reaction of reactant to product. The pressure-dependent rate of depletion of the reactant is

$$R(\lambda, P) = K \left(\frac{P}{P_{VN}}\right)^{\nu} (1-\lambda)^{1/2}, \tag{3}$$

where K is the rate multiplier, P_{VN} is the von Neumann pressure (defined in Section 5), and ν is an adjustable parameter, typically $0 < \nu < 5$.

In the remainder of the paper, pressure is expressed in GPa, speed in km/s, density in cc/g, specific volume in g/cc, energy in kJ/g, time in μs, and distance in mm.

3.2 Equation of state

To close the system of equations above, it is necessary to relate pressure P, specific volume $v = 1/\rho$, and internal energy e through an equation of state. The most popular of such thermodynamic relations for compressible flow is the perfect gas equation of state, $P(e, v) = (\gamma - 1)\, e/v$, where γ is the ratio of specific heats.

In the solid state (or in a dense fluid regime), pressure can be expressed as the sum of two terms, $P(e, v) = P_T + P_C$ [62]. The thermal component P_T is associated with the random motion of atoms and molecules and is related to the heat capacity $C_v(T) = (\partial e/\partial T)_v$. P_T is the only pressure component acting in a gas. The cold component P_C is due to intermolecular forces, repulsive at short distances and attractive at long distances. The cold component of pressure dominates the thermal component for the higher compressed state produced in solid explosive detonations [61]. P_C and the associated cold compression energy e_C are evaluated at absolute zero temperature and, therefore, are only a function of v.

An important thermodynamic property of a solid is the Grüneisen parameter $\mathcal{G}$ [62, 5, 33],

$$\mathcal{G} = v \left(\frac{\partial P}{\partial e}\right)_v. \tag{4}$$

A typical approximation is to assume that the Grüneisen parameter is dependent only on the specific volume, as in

$$\mathcal{G}(v) = \mathcal{G}_0 \left(\frac{v}{v_0} \right)^q,$$

where $\mathcal{G}_0$ and q depend on the material (see, for instance, [34]). The Mie-Grüneisen equation of state is formulated as

$$P(e, v) \sim \mathcal{G}(v) \frac{e - e_C(v)}{v} + P_C(v) = \mathcal{G} \frac{e}{v} + f(v). \tag{5}$$

For a perfect gas, $\mathcal{G}(v) = \gamma - 1$ and $f(v) = 0$. For condensed phase materials, expressions for $\mathcal{G}$, e_C, and P_C must be obtained from experiments or molecular dynamics simulations [17].

3.2.1 Shock wave data

An alternative to using the cold compression functions e_C and P_C in equation (5) is provided by shock compression data. Shock experiments on solids provide a relation between the shock speed U_s and the particle velocity behind the shock, u_p, along the locus of shocked states (the Hugoniot of the inert material). For non-porous materials, and in the absence of phase transitions, these data are approximated reasonably well by a linear relation

$$U_s = c_0 + s\, u_p. \tag{6}$$

In equation (6), c_0 is the bulk sound speed at ambient conditions and s is related to the isentropic pressure derivative of the isentropic bulk modulus, $K_s' = \partial K_s / \partial P|_s$, through the formula $s = (K_s' + 1)/4$ (see [34]).

By neglecting ambient pressure P_0 and internal energy e_0 with respect to the compressed states, the pressure $P_\mathcal{H}$ and the internal energy $e_\mathcal{H}$ on the Hugoniot (figure 2) are obtained from the shock jump conditions and the linear relation (6) as

$$P_\mathcal{H} = \rho_0 U_s u_p = \rho_0 c_0^2 \frac{\varphi}{(1 - s\varphi)^2} \tag{7}$$

and

$$e_\mathcal{H} = \frac{P_\mathcal{H}}{2}(v_0 - v), \tag{8}$$

with $\varphi = 1 - v/v_0$. By using the definition of $\mathcal{G}$ and an approximate expansion of $P(e, v)$, we can write

$$P(e, v) \sim \mathcal{G} \frac{e - e_\mathcal{H}(v)}{v} + P_\mathcal{H}(v). \tag{9}$$

The Hugoniot-based Mie-Grüneisen equation of state is, therefore,

$$P(e, v) = \frac{\mathcal{G}}{v} e + \frac{\rho_0 c_0^2 \varphi}{(1 - s\varphi)^2} \left[1 - \frac{\mathcal{G}}{2v}(v_0 - v) \right]. \tag{10}$$

By comparison with (5),

$$f(v) = P_\mathcal{H} \left[1 - \frac{\mathcal{G}}{2v}(v_0 - v) \right]. \tag{11}$$

The sound speed, defined [54] as

$$c^2 = \left(\frac{\partial P}{\partial \rho}\right)_e + \frac{P}{\rho^2}\left(\frac{\partial P}{\partial e}\right)_\rho, \tag{12}$$

can be expressed as

$$c^2 = \mathcal{G}e + \frac{\partial f}{\partial \rho} + \mathcal{G}\frac{P}{\rho}. \tag{13}$$

3.2.2 Expanded states

Expanded states below the reference point can occur for sufficiently strong rarefactions. An example of this is given later in the discussion on shock diffraction around a corner. The expressions (10) and (11) are no longer valid for $v > v_0$, since, on the shock adiabat, $v < v_0$. Attempting to simply extrapolate (10) to expanded states eventually fails because the square of the sound speed can become negative for realistic values of ρ and e. A solution is to modify the function f to be

$$f(v) = c_0^2\left(\frac{1}{v} - \frac{1}{v_0}\right) \quad \text{if} \quad v > v_0. \tag{14}$$

This is similar to the pseudo-elastic approximation used by Miller and Puckett [34] to eliminate analogous difficulties in their computations. Thus, the final form of our expression for f is

$$f(v) \quad = \begin{cases} \dfrac{\rho_0 c_0^2 \varphi}{(1-s\varphi)^2}\left[1 - \dfrac{\mathcal{G}}{2v}(v_0 - v)\right] & \text{if} \quad v \le v_0 \quad \text{(a)} \\ c_0^2\left(\dfrac{1}{v} - \dfrac{1}{v_0}\right) & \text{if} \quad v > v_0 \quad \text{(b)} \end{cases} . \tag{15}$$

Note that f is not defined for $v \le v_a = v_0(s-1)/s$. This is the minimum specific volume allowed by the linear U_s–u_p relation.

3.2.3 Isentropes

By substituting equation (5) in the isentropic relation $de = -Pdv$, we obtain the following non-homogeneous ordinary differential equation (ODE) for internal energy on an isentrope

$$\frac{de}{dv} + \mathcal{G}\frac{e}{v} = -f. \tag{16}$$

The solution, passing through a reference state defined by (e_i, v_i), is

$$e_s(v) = e_i\left(\frac{v}{v_i}\right)^{-\mathcal{G}} - v^{-\mathcal{G}}\int_{v_i}^{v} f v^{\mathcal{G}} dv.$$

By substituting $e_s(v)$ in equation (5), we obtain the isentropic pressure

$$P_s = -\frac{\mathcal{G}}{v^{\mathcal{G}+1}}\int_{v_i}^{v} f v^{\mathcal{G}} dv + \mathcal{G}\frac{e_i v_i^{\mathcal{G}}}{v^{\mathcal{G}+1}} + f. \tag{17}$$

Closed-form solutions of the integral are not possible for arbitrary $\mathcal{G}$. In our examples, P_s is computed using Romberg's numerical integration [41]. This iterative technique provides high accuracy for sufficiently smooth functions. If $\mathcal{G}$ is an integer, it is a matter of simple calculus to provide a closed-form expression for P_s.

Example isentropes are shown in figures 3(a) and (b) using $\mathcal{G} = 2$ and the remaining parameters from table 3. These cases do not correspond to any real material, but were selected to verify the numerical results against closed-form integration of equation (17). Note that in figure 3(a), $P_s(v)$ exhibits an inflexion point. An interesting implication of this is discussed in Section 5.3. Results for more realistic values of the Grüneisen parameter are displayed in figure 4.

We conclude this section by deriving expressions for the sound speed c,

$$c^2 = -v^2 \left(\frac{\partial P}{\partial v}\right)_s, \tag{18}$$

and for the fundamental derivative of gasdynamics Γ [54],

$$\Gamma = \frac{v^3}{2c^2} \left(\frac{\partial^2 P}{\partial v^2}\right)_s. \tag{19}$$

Substitution of equation (10) in the previous definitions gives

$$\left(\frac{\partial P}{\partial v}\right)_s = -\mathcal{G}\left[\frac{f}{v} - \frac{(\mathcal{G}+1)}{v^{(\mathcal{G}+2)}} \int_{v_i}^{v} f v^{\mathcal{G}} dv\right] - \mathcal{G}\,(\mathcal{G}+1)\,\frac{e_i v_i^{\mathcal{G}}}{v^{(\mathcal{G}+2)}} + f' \tag{20}$$

and

$$\left(\frac{\partial^2 P}{\partial v^2}\right)_s = \frac{(\mathcal{G}+2)}{v}\left(\frac{\partial P}{\partial v}\right)_s - f'\left(\frac{\mathcal{G}}{v}+1\right) + f''. \tag{21}$$

4 Numerical integration of the Euler equations

The reactive equations (1) are numerically integrated by using the time splitting technique proposed by Strang [51]. In the operator splitting procedure, the homogeneous Euler equations

$$\mathbf{U}_t + \nabla \cdot \mathbf{F}(\mathbf{U}) = \mathbf{0}, \tag{22}$$

and the system of ODEs

$$\mathbf{U}_t = \mathbf{\Omega}(\mathbf{U}), \tag{23}$$

are computed separately. $\mathbf{F}(\mathbf{U})$ is the vector of the convective fluxes and $\mathbf{U}$ is the vector of conservative variables. In terms of the advection operator $\mathcal{L}_A$ and the chemistry operator $\mathcal{L}_C$, the Strang's splitting takes the form

$$\mathbf{U}^{n+1} = \mathcal{L}_C\left(\frac{\Delta t}{2}\right)\,\mathcal{L}_A\left(\Delta t\right)\,\mathcal{L}_C\left(\frac{\Delta t}{2}\right)\,\mathbf{U}^n. \tag{24}$$

By recursion, equation (24) may be written as

$$\mathbf{U}^{n+1} = \mathcal{L}_C\left(\frac{\Delta t}{2}\right)\,\mathcal{L}_A\left(\Delta t\right)\,\mathcal{L}_C\left(\Delta t\right)\cdots\mathcal{L}_A\left(\Delta t\right)\,\mathcal{L}_C\left(\frac{\Delta t}{2}\right)\,\mathbf{U}^0. \tag{25}$$

Tang [52] provides error estimates for stiff ODE operators when the solution to the homogeneous advection equations is exact. To maintain the overall order of accuracy in the time integration, one should carry out the first and last iterations with only half the value of the time step. For simplicity, we do not perform the first halved time step ODE iteration and perform a whole time step in the last ODE iteration. This approximation is, in general, acceptable for n large.

The multi-dimensional finite volume discretization of (22) is based on the integral formulation of the conservation equations

$$\frac{\partial}{\partial t}\int_{\mathcal{C}_i} \mathbf{U}\,\mathrm{d}\mathbf{x} + \int_{\partial\mathcal{C}_\mathrm{i}} \mathbf{F}(\mathbf{U})\cdot\mathbf{n}\,\mathrm{dl} = 0, \tag{26}$$

where $\mathcal{C}_i$ is the control volume, $\partial\mathcal{C}_i$ is its boundary, $\mathrm{d}\mathbf{x}$ is the volume element, dl is the boundary element, and $\mathbf{n}$ is the outward normal unit vector to $\partial\mathcal{C}_i$.

The literature abounds with methods to properly approximate at the cell interface the numerical flux $\Phi_{i+1/2}(\mathbf{U}_{i+1}, \mathbf{U}_i)$ needed by equation (26). For stability reasons, this flux must be upwind, or appropriate dissipation must be added to a central scheme. Upwind schemes include those proposed by Godunov [18], where the exact Riemann problem is solved at the cell boundary, by Roe [43], who uses a linearized solver based upon the sign of the eigenvalues of the Jacobian of the convective fluxes, by van Leer [57], who uses a flux splitting based upon the value of the local Mach number, and by Shu and Osher [47], with the Essentially Non Oscillatory (ENO) solver based on interpolation via divided difference tables. This list is certainly not exhaustive, but indicates the range of the different methods available. One must note that all those methods were initially developed for perfect gases. Several were extended to the more complex case of real gases [46, 28], but only a few, it appears, were used for solid-state materials.

A Godunov solver, where the approximate and non-iterative solution of the Riemann problem requires only two material-dependent parameters, was developed by Dukowicz for a general equation of state [8]. This approach was successfully extended by Miller and Puckett [34] to a multi-phase scheme that is second-order accurate in regions of smooth flow. The thermodynamic model was based on the Mie-Grüneisen equation of state and tested in the context of shock wave geophysics. The description of a two-phase approximate Godunov solver with a non-ideal Tait solid can be found in [20]. Saurel and Massoni [45] used the HLL solver by Harten, Lax, and van Leer [22], with the modification suggested by Toro [56], to solve the Riemann problem with two distinct Mie-Grüneisen equations. Numerical studies by Vitello et al. [58] on the HLL scheme investigated the role of artificial viscosity in Arbitrary Lagrangian Eulerian (ALE) computations of detonations with JWL equation of state. Fedkiw et al. used an ENO solver in examples computed with the Tait equation of state in [11, 10]. Finally, Xu and Stewart extended the use of ENO to a non-conservative system of equations derived for a single-velocity two-phase model of high explosive [60].

In the present study, we use the extension proposed by Glaister [16] of Roe's method. Roe's scheme has a few flaws, such as capturing unphysical expansion shocks in gases or the "carbuncle" phenomenon, but these flaws are well known and most of them can be corrected [21, 44]. The one-dimensional expression for the numerical flux is

$$\mathbf{F}(\mathbf{U})\cdot\mathbf{n} \approx \Phi^{\mathrm{Roe}}_{i+1/2}(\mathbf{U}_{i+1}, \mathbf{U}_i) = \frac{1}{2}\left[\mathbf{F}_i + \mathbf{F}_{i+1} - |A_{i+1/2}|\,(\mathbf{U}_{i+1} - \mathbf{U}_i)\right], \tag{27}$$

where the dissipation matrix A is the Jacobian of $\mathbf{F}$, $A = \mathrm{D}_{\mathbf{U}}\mathbf{F}$. Expressions for A and the associated eigenvectors can be found in [48]. Roe [43] has shown that A must be evaluated at the following averages

$$\begin{aligned} \overline{\rho} = \rho_{i+1/2} = \sqrt{\rho_i\,\rho_{i+1}} \qquad & \overline{\beta} = \beta_{i+1/2} = \frac{\sqrt{\rho_i}\,\beta_i + \sqrt{\rho_{i+1}}\,\beta_{i+1}}{\sqrt{\rho_i} + \sqrt{\rho_{i+1}}} \\ \overline{P} = P_{i+1/2} = \overline{\rho}\left(\overline{H} - \overline{e} - \frac{1}{2}\overline{u}^2\right) \qquad & \overline{c}^2 = c^2_{i+1/2} = \frac{\overline{P}\,\overline{P}_e}{\overline{\rho}^2} + \overline{P}_\rho, \end{aligned} \tag{28}$$

where $\beta = u$, e, and H. The Roe average is also performed for the mass fraction, i.e., $\beta = \lambda$ in (28). The partial derivatives of pressure, P_ρ, P_λ, and P_e, at a cell interface are computed as linear averages of the derivatives on each side of the interface. Harten's entropy correction [21] is added to all the waves.

The scheme is rendered Total Variation Diminishing (TVD) by a minmod limiter [53]. The minmod limiter may be replaced by Roe's "Superbee" limiter [53], or any other technique that will damp out spurious oscillations.

Time marching of the advection operator is achieved through explicit time stepping. In one dimension

$$\mathbf{U}_i^{n+1} = \mathbf{U}_i^n - \Delta t\,\left(\mathbf{\Phi}_{i+1/2} - \mathbf{\Phi}_{i-1/2}\right),$$

where the time step Δt accounts for the stability condition

$$\Delta t = \mathit{CFL}\,\frac{\Delta x}{|u| + c}.$$

CFL is the Courant-Friedrichs-Levy number, Δx is the space discretization, u is the fluid velocity, and c is the speed of sound.

Time marching of the chemistry operator reduces to the integration of

$$\frac{d}{dt}\begin{pmatrix} \rho \\ \rho\mathbf{u} \\ \rho E \\ \lambda \end{pmatrix} = \begin{pmatrix} 0 \\ \mathbf{0} \\ 0 \\ R(\lambda, P) \end{pmatrix}. \tag{29}$$

Since the conserved quantities in (29) remain constant in the interval Δt, we need only to integrate the equation for the mass fraction and correct its advected value obtained from (22).

The simulations presented in this work are performed with the adaptive mesh refinement (AMR) capability provided by the Amrita computational facility of Quirk [42]. AMR is especially useful for correctly capturing flow features such as contact discontinuity and reaction zones.

5 The shock tube problem

A shock tube consists of two materials at two different pressures, P_1 and P_4, separated by a membrane (see Figure 5, where $P_1 < P_4$). When the membrane ruptures, three waves are

generated: a shock, a contact discontinuity, and a rarefaction [54]. This Riemann problem may be solved exactly using the Riemann invariants and the shock jump conditions. The material on the right of the membrane is shock-compressed to state 2, according to the shock speed U_s. The material on the left experiences an isentropic rarefaction whose final value is given by state 4. State 2 and 3 have equal pressure (mechanical equilibrium) and velocity (no discontinuity in the material) but can be separated by a discontinuity in density.

5.1 An exact solution to the shock tube problem

In this section, we compute the solution of the shock tube problem for a single material obeying the Mie-Grüneisen equation of state. While this solution exists in closed form for a perfect gas [54], numerical integration and the iterative evaluation of non-linear equations are required for the Mie-Grüneisen case. This "exact" solution will be compared in the next section with the results obtained with the linearized Roe-Glaister solver.

The solution is obtained by iteration, adjusting the shock velocity until the conditions across the contact discontinuity are satisfied. Graphically, this corresponds to finding the common point $P_2 = P_3$ and $u_2 = u_3$ that corresponds to the state of the contact between the rarefaction fan and the shock. This point is at the intersection of the rarefaction wave passing by the compressed state (P_4, v_4) with the shock Hugoniot passing by the rest state (P_1, v_1).

Briefly, the algorithm starts with an initial guess for the shock velocity U_s. Using the shock jump conditions and an initial value for v_2, we find the shock-compressed state (P_2, e_2). Since P_2 must satisfy the Mie-Grüneisen equation of state, v_2 is iterated until $P_2 = P(e_2, v_2)$. In this way, the post-shock state is computed for the given U_s. Then, we use the matching condition at the contact discontinuity $P_3 = P_2$ to iteratively find the value v_3 such that P_3 equals the value $P_s(v_3)$ of the pressure isentrope passing by state 4. Next, the Riemann invariant is used to find the change in velocity across the rarefaction

$$u_3 = u_4 + \int_{v_4}^{v_3} \sqrt{-\left(\frac{\partial P}{\partial v}\right)_s} dv, \tag{30}$$

by carrying out the integration with Romberg's technique. At this point, the second matching condition $u_3 = u_2$ closes the problem. If $u_2 > u_3$, the value of U_s is decreased and if $u_2 < u_3$, U_s is increased. We repeat this process until $|u_2 - u_3| < \epsilon$, the prescribed error. Overall, this algorithm may be regarded as an implementation of the Newton method to find U_s given states 1 and 4. As such, it will converge if the initial guess for U_s is not too far off the solution. Figure 6 shows both the Hugoniot and the isentropic pressure in the (P, u) plane. The point at the intersection of the two curves, represented by a solid diamond, is computed by the algorithm described above.

Once U_s is known, we can find the specific volume and velocity inside the rarefaction fan, v_r and u_r, using the Riemann invariant between the backward characteristics of inverse slope, $u_4 - c_4$ and $u_3 - c_3$. For the characteristic with specific volume v_r, $v_4 < v_r < v_3$, we compute the velocity with equation (30) and the sound speed with $c_r^2 = -v_r^2 \left(\partial P/\partial v\right)_s (v_r)$, and then find the location $x_r(t) = t\,(u_r - c_r)$ where the flow takes the values v_r, u_r and $P_r = P_s(v_r)$.

In the rest of this paper, we will refer to this algorithm as our "exact" Riemann solver, exact meaning that this solution is correct up to the precision allowed by the Newton method and the numerical integration method. This algorithm, too cumbersome to be used for calculating numerical fluxes, provides in the next section a reference solution to validate our numerical time-dependent finite-volume simulation.

5.2 Non-reactive shock tube experiments

Results of shock tube simulations are compared against the exact solutions for Kel-F and HMX_sp in figures 7 and 8. The thermodynamic properties of the two materials are given in table 3. The approximate solution is computed on a uniform grid $\Delta x = 10^{-3}\,\mathrm{mm}$ for both cases. From the very favorable agreement between the exact solution (solid line) and the approximate solution (open diamonds), we conclude that the Roe-Glaister solver is suited for use in shock dynamics computations for materials described by the Mie-Grüneisen equation of state.

5.3 Rarefaction shock

Before concluding this section, we examine the artificial situation where a material similar to Kel-F (table 3) has a larger $\mathcal{G}$ coefficient. Figures 9(a) and (b) show the fundamental derivative Γ computed for $\mathcal{G} = 2$ and $\mathcal{G} = 1.7$. Negative values of Γ are of particular interest since they can give rise to expansion shocks. This is seen by expressing Γ as

$$\Gamma = 1 + \frac{\rho}{c}\left(\frac{\partial c}{\partial \rho}\right)_s. \tag{31}$$

From the theory of characteristics [54],

$$d\left(\frac{dx}{dt}\right)_{C^\mp} = \mp\,\frac{\Gamma}{\Gamma - 1}\,dc. \tag{32}$$

In equation (32), $(dx/dt)_{C^\mp} = (u \mp c)$ is the inverse slope of the $C^\mp$ characteristics in the x–t plane and $d(\cdot)$ is the variation taken along the family of opposite characteristics. If $\Gamma < 0$, then stronger rarefaction waves travel faster than weak ones, leading to the convergence of expansion characteristics and, eventually, to an expansion shock. Under these conditions, an expansion shock may be a legitimate (i.e. entropy non-decreasing), solution to the Euler equations, just as compression shocks are for ordinary materials. Expansion shocks are experimentally observed in certain regimes in multi-phase dense gases [55], and predicted and computed to occur in single-phase dense gases [13, 12]. Expansion shocks cannot occur in perfect gases, where $\Gamma = (\gamma + 1)/2$, because γ is always positive.

Figure 10 shows the isocontours of negative Γ for various values of (P, v). This area, close to the limit specific volume v_a defined in Section 3.2.2, cannot be neglected for $\mathcal{G} = 2$, but is very small for $\mathcal{G} = 1.7$. For the more realistic case $\mathcal{G} = 0.45$, Γ remains positive in the entire (P, v) range of interest.

A few modifications to the original algorithm are required in order to account for expansion shocks. The fundamental derivative, computed with equation (19), must be monitored

inside the expansion fan for negative values. If applicable, shock jump conditions must be used to compute U_{es}, the expansion shock velocity, and P_4^{new}. In general, the pressure evaluated from shock jump conditions across the expansion shock is not necessarily equal to P_4, so that the computation of the rarefaction should be embedded in a loop over the value of U_s.

Figure 11 shows the exact solution of the shock tube problem, the plot of Γ, and the approximated solution (for $\Delta x = 5 \cdot 10^{-3}\,\text{mm}$). Close to the rarefaction head, where the fundamental derivative is negative, the exact solution (solid line) exhibits a weak expansion shock. Its correct position is found with only one iteration, since we found $|P_4^{\text{new}} - P_4|/P_4 = 1.60 \cdot 10^{-5}$ at the first pass. As in the previous example, the solution obtained from the Roe-Glaister solver (diamonds in Figure 11) follows the exact solution very well, and correctly captures the weak expansion shock.

6 Shock diffraction

In this section, we present results of two-dimensional shock diffraction in an inert solid with the model parameters appropriate to HMX_sp. The problem consists of a traveling shock wave that diffracts around a sharp corner. The abrupt area change generates rarefaction waves departing from the corner followed by complex vortex-shock interactions.

In numerical simulations of a gas, strong rarefactions can result in negative pressures. A gas does not support tension, and clearly negative pressures are unphysical, but the most serious consequence is that for a perfect gas, $c^2 = \gamma\, P/\rho$, and negative pressures result in negative c^2, causing a numerical simulation to abort. From experience, this problem does not occur in perfect gases for Mach numbers no greater than 2.5 when Roe's entropy corrected scheme is used [21]. The entropy correction adds enough dissipation to the scheme to avoid the problem. Higher Mach numbers usually require more dissipative flow solvers that will not be described here (see Quirk [42]).

Solids, however, can support tension provided the stresses are less than the limit value associated with fracture. For these cases, explicit extensions of the equation of state are required so that the square of the sound speed remains positive for negative pressures. In the following example, we test our Roe-Glaister solver with the Mie-Grüneisen model expanded to treat tension, as discussed in Section (3.2.2).

6.1 Geometry

The computational domain is an 80 mm $\times$ 80 mm square, containing 80 $\times$ 80 coarse cells. It includes a step that extends 30 mm in width (x-direction) and 50 mm in height (y-direction). Adaptive refinement targets the variation of density to identify steep gradients or contact discontinuities. With R and L denoting the right and left sides of a cell interface, the two criteria,

$$\frac{|\rho_R - \rho_L|}{\rho_R + \rho_L} > \frac{|P_R - P_L|}{P_R + P_L} \tag{33}$$

and

$$\frac{|\rho_R - \rho_L|}{\rho_R + \rho_L} > \varepsilon\,, \quad \varepsilon << 1, \tag{34}$$

are used in sweeps of the grid in the two Cartesian directions [42]. To avoid the amplification of start-up errors, the more stringent refinement criterion (33), used to capture contact discontinuities, is performed only later in the run. Three levels of refinement, each with refinement ratio 2, are maintained throughout the simulation, so that the smallest grid size is $\Delta x = 0.125$ mm.

We initialize the data with post-shock values to the left of the wave. The shock is located at $x_s = 5$ mm and has speed $U_s = 9.60$ km/s, corresponding to a shock Mach number $M_s = U_s/c = 3.13$. This gives the post-shock state $P = 66.17$ GPa and $\rho = 3.05$ g/cc.

The approximate solver generates spurious start-up oscillations due to the evolution of the ideal initial jump to the actual shock profile. To remove these oscillations the code is initially run for 1.56 μs until the shock front has moved 10 mm in the channel. Then the solution behind the shock front is "repainted" with the numerical post-shock values (arbitrarily taken at 5 mm from the numerical front).

6.2 Numerical results

Figure 12 shows the solution at time $t = 1.56$ μs and $t = 3.55$ μs in the form of numerical Schlieren images based on the modulus of the density gradient. The solution at the final time $t = 7.49$ μs is shown in Figure 13. In frame (a), the refinement flags indicate where the AMR algorithm is active. In frame (b), one can count at least two shocks in the vortex region interacting with the contact discontinuity that forms at the corner. Due to the very low pressures in the core of the vortex, the extended equation of state described in Section 3.2.2 is accessed by the solver.

To evaluate the performance of the extended equation of state, we look at the cross-sections of the flow field at $x = 31$ mm and $x = 32$ mm at time $t = 3.55$ μs. Frames (a) to (d) in figure 14 show density and pressure as a function of y, whereas frames (e) and (f) show pressure as a function of density. Frames to the left of the figure correspond to $x = 31$ mm, while frames to the right correspond to $x = 32$ mm. In all the plots, the open diamond curve is the rest state at 1.56 μs and the cross represents the solution at 3.55 μs. The lowest density in frame (a) is approximately ~ 0.66 g/cc, corresponding to -5 GPa in frame (c). Pressure is always positive in the cross-section at $x = 32$ mm, since the vortex core is located further to the left. Note that, in the two pressure-volume plots, data points are mostly distributed along the shock Hugoniot curve, as expected, and that in frame (e) the portion of the curve extended to negative pressures is also visible.

7 A simple detonation model

In analogy with the simplest model of reactive perfect gas, a simple detonation model for a solid explosive can be obtained by adding an energy release term to the Mie-Grüneisen equation of state. The resulting equation,

$$P = \mathcal{G}\frac{e}{v} + f(v) + \mathcal{G}\frac{\lambda\, q}{v}, \tag{35}$$

is well suited for implementation in a numerical solver because it provides an explicit dependence on the mass fraction of the products λ. The energy release q represents the heat

of reaction released in the transformation of reactants to products. Its value can be chosen to match the experimental value of the CJ propagation speed, U_{CJ}, or the pressure at the CJ state, P_{CJ}, but, in general, not both conditions at the same time. A better match to product properties could be obtained by making $\mathcal{G}$ a function of the state of the products. For instance, it is well known that the value $\mathcal{G}$ is close to 2 for detonation products near the CJ point and then decreases to approximately 0.3 at lower pressures. We have not explored this potentially more accurate approach as our goal in the present study was to extend the Mie-Grüneisen model in the simplest way possible.

To derive the relation between q and U_{CJ}, we take a control volume bounded by the shock and any point in the reaction zone inside the one-dimensional CJ wave. If the values P_0 and e_0 of the material at rest can be neglected with respect to the values in the reaction zone, conservation of energy is expressed as

$$e = \frac{1}{2} P \left(v_0 - v \right). \tag{36}$$

Using the reactive equation of state (35), with $\lambda = 1$, to substitute e as a function of P, v and q yields the reactive version of the p–v representation of the Hugoniot,

$$P_{\mathcal{H}}(v) = \frac{f(v) + \frac{\mathcal{G}}{v} q}{1 - \frac{\mathcal{G}}{2v} \left(v_0 - v \right)}, \tag{37}$$

which is the extension of equation (11) to reactive flow.

Another representation of the Hugoniot can be found by using momentum conservation, $P = u_p U_s / v_0$, and mass conservation, $v = v_0(1 - u_p/U_s)$, to obtain an implicit relation between u_p and U_s.

$$2\,\mathcal{G}\,q \left(U_s - s u_p \right)^2 - u_p \left(2U_s - (2 + \mathcal{G})\, u_p \right) \left(\left(U_s - s u_p \right)^2 - c_0^2 \right) = 0. \tag{38}$$

The corresponding U_s–u_p diagram is shown in figure 15 with q as a parameter. When $q = 0$, the linear U_s–u_p relation of equation (6) is recovered. When $q > 0$, the curve has a point that is tangent to the horizontal Rayleigh line. This minimum corresponds to the CJ state for that particular value of q [14] and can be found by differentiating equation (38) with respect to u_p, keeping $\partial U_s / \partial u_p = 0$. This procedure leads to a non-linear equation in U_s and u_p that can be solved numerically, yielding the CJ wave velocity $U_{CJ} = U_s \left(u_{p,min} \right)$.

Figure 15 also shows shock compression data for single-crystal and solvent-pressed HMX [32], as well as detonation data for the HMX-based explosives PBX 9404 and PBX 9501 [50]. These data suggest that at high compression the U_s–u_p curve for HMX is less steep than the curve obtained with the values c_0 and s in table 3.

The overall agreement of our model with the data in figure 15 is rather poor, even if there is a qualitative correspondence near the CJ state (we do not access overdriven states in the simulations presented here). Note also that the CJ speed for PBX 9404-9501 is slightly smaller than the CJ speed for HMX_sp. Excellent agreement is instead obtained by more complex equations of state that are directly calibrated on the experimental data. This is shown by the two additional U_s–u_p diagrams in figure 15, calculated from the model for PBX reactants and products proposed by Stewart, Yoo, and Davis [50]. With more complex models, the number of required parameters tends also to increase. In this example, twelve

Table 2: JWL parameters for HMX products.

A [GPa]	B [GPa]	C [GPa]	R_1	R_2	ω	v_0 [cc/g]
778.3	7.071	0.643	4.20	1.	0.3	0.5288

parameters where used for computing the two U_s–u_p diagrams for PBX, versus the four parameters (c_0, s, $\mathcal{G}$, and q) appearing in equation (38).

The measured CJ state for HMX_sp is $U_{CJ,\,exp} = 9.11\,\mathrm{km/s}$ and $P_{CJ,\,exp} = 39.0$ GPa [7]. As anticipated, we find that in our model either the correct CJ speed is obtained (with $q = 12.67\,\mathrm{kJ/g}$) at a smaller CJ pressure $P_{CJ,\,calc} = 34.48$ GPa (figure 16(a)); or the correct CJ pressure is obtained (with $q = 14.67\,\mathrm{kJ/g}$) at a larger wave speed $U_{CJ,calc} = 9.60\,\mathrm{km/s}$ (figure 16(b)). In the end, since the sensitivity of the reaction rate to the local thermodynamic state is built in our model via a pressure dependence, and we are interested here in comparing simulations with pressure-insensitive and pressure-sensitive reaction rates, we decided to use the value $q = 14.67\,\mathrm{kJ/g}$.

The ZND profile corresponding to $q = 14.67\,\mathrm{kJ/g}$ is shown in figure 17 for $\nu = 5$, $K = 2$, and the values listed in table 3. The wave is computed by numerical quadrature of the differential equations derived from the set (1) in the one-dimensional steady case.

We conclude this discussion by comparing the isentropic pressure derived from our model with the JWL fit

$$P_{s,JWL}(v) = Ae^{-R_1 v/v_0} + Be^{-R_2 v/v_0} + C(v/v_o)^{-\omega-1} \tag{39}$$

for HMX products [7]. The JWL parameters for HMX are listed in table 7. The Mie-Grüneisen isentrope for HMX products is obtained by substituting $f + \mathcal{G}\,q/v$ to f in equation (17). The reference volume in the equation is chosen to be $v_i = 0.43\,\mathrm{cc/g}$, close to the CJ value. The reference pressure P_i is computed directly from (39), so that the two isentropes are centered on the same state. Figure 18 shows that the curves are approximately tangent at that point and also remain relatively close to each other for larger volumes. The behavior of the product equation of state in the pressure range between 0 and 10 GPa, shown in figure 18 (b), is particularly important when computing products expansion in problems such as cylinder test simulations and other configurations that are relevant to accelerating materials.

7.1 Reactive shock tube computation

In the setting of this shock tube problem, the fluid to the left of the membrane is pressurized to P_{VN}, while the fluid to the right is set at the rest state. The reaction rate is given by equation (3), with $\nu = 5$ and $K = 2$. The computation is carried over a regular grid with $\Delta x = 1.3\,\mathrm{mm}$. Figure 19(a) shows pressure as a function of distance at regular time intervals. To the right, pressure first drops from P_{VN} to P_{CJ}, then climbs back to P_{VN} as a self-sustaining detonation progresses through the tube. To the left of the membrane, a rarefaction wave reaches the left wall, where reflective boundary conditions are implemented, and reflects as a new rarefaction wave. A second rarefaction extends from the end of the reaction zone to equilibrate the pressure reached at the contact discontinuity. Figure 19(b)

shows the first and the last pressure diagrams, at $t = 0\,\mu$s and $t = 18.4\,\mu$s. P_{VN} and P_{CJ} are slightly underestimated by the approximate solver, indicating that a finer grid is required in the reaction zone, but, overall, the detonation wave appears to propagate as the correct ZND-CJ profile.

7.2 Reactive shock diffraction with pressure-independent rate

The geometry shown in Figure 20 is the same as that described for non-reactive flow. Data are initialized by computing the reference ZND profile for the steady state CJ wave with $\nu = 0$ and $K = 2$. The solution is then copied as a plane wave in the computational domain. This procedure is identical to the one used in our previous computation of inert shock diffraction in Section 6. The same technique to remove start-up errors as used with inert shocks is also used for detonations.

This computed reaction zone is labeled "Detonation" in Figure 20. The burnt gases, labeled "Products", are at the CJ state behind the reaction zone and the rear boundary is implemented as a Dirichlet conditions at the CJ state. The corner is assumed to be rigid and inert (modeled by standard reflective boundary conditions). To the right of the reactants, there is a higher density inert substance, defined by $\rho = 1.5\,\rho_0$, $\lambda = 1$ and $P = P_0$.

The computational domain measures 423 mm × 211 mm. At start-up, the entire reaction zone of the reference ZND-CJ profile, between $\lambda = 0$ and $\lambda = 1$, contains 20 computational cells in a 6.60 mm long reaction zone. This length is, of course, unrealistically large for HMX and was chosen for convenience in this example problem. Refinement is based on the mass fraction gradient and the density gradient. The reaction zone is always embedded in grid patches with the highest allowed level of refinement, so that the initial grid resolution is maintained in the AMR calculation.

Figure 21 shows the detonation wave diffracting around the corner and eventually interacting with the higher density inert substance. The incident shock is partially transmitted through the inert material and partially reflected. The transmitted wave passes through the right boundary of the domain, where transmissive boundary conditions are implemented, while the reflected wave interacts with the vortex formed at the corner. The lower part of the diffracted wave reflects from the bottom of the domain (with reflective boundary conditions) and moves upward to interact with the vortex at a time close to $t = 42.77\,\mu$s. At the final time $t = 55.89\,\mu$s, a system of transmitted and reflected waves can be observed surrounding the vortex, while the contact line formed between the corner and the vortex core is quite diffuse. In the last frame of figure 21, the AMR algorithm loses track of the shock aligned with the grid. This could have been avoided by decreasing the tolerance of the refinement criteria, but only at the price of a greater computational overhead. Details of a few flow features are shown in figures 22, 23, and 24. Boxes in the figures to the left show where the close-ups are performed.

7.3 Reactive shock diffraction with pressure-dependent rate

We now consider the pressure-dependent reaction rate case, equation (3), $\nu = 5$ and $K = 2$. The initialization and overall set-up of the experiment are the same as in the fixed-rate computation. The reaction zone measures 26.29 mm, approximately four times the reaction

length in the pressure-insensitive case. To compare the results with the previous case, the domain size is scaled to be four times larger, 1683 mm × 841 mm.

Figures 25, 26, and 27 show a comparison between the fixed and pressure-dependent rates computations. Each plot is taken at the time when the incident wave has covered the same distance measured with respect to the reference reaction zone length. In each figure, the top frames are numerical Schlieren images, while the bottom plots are isocontours of λ.

The diffracted wave considerably slows down in the case of the pressure-dependent rate. This is due to the fact that when the pressure ratio P/P_{VN} becomes sufficiently small, the reaction essentially subsides. Chemical reaction is no longer sustained behind the shock and a region of partially reacted explosive is left close to the vertical corner wall – the so-called "dead-zone" (see [30] and references therein).

Summary

In this work, we have investigated the numerical solution of compressible flow in solids using the Mie-Grüneisen model together with numerical methods that were originally introduced for gas dynamics problems. To verify our work, we have developed a numerical procedure to obtain similarity solutions for the shock tube problem using the Mie-Grüneisen equation of state. We implemented a Roe-Glaister solver and verified that it computes this Riemann problem correctly. We then used it to simulate the two-dimensional corner-turning problem in inert HMX_sp. This study demonstrated the necessity of an extended equation of state to account for tension. We proposed a rudimentary extension to the Mie-Grüneisen equation and applied it successfully to this test case.

A simple detonation model was implemented in the Mie-Grüneisen equation of state. This is based on a constant energy release and is analogous to the model commonly used for gaseous detonations. The shock tube and corner-turning problems were computed again, this time for reactive HMX. One of these simulations, with pressure-dependent reaction rate, enabled us to visualize the formation of a "dead-zone" region along the wall downstream of the corner.

We conclude by reporting that Morano and Shepherd recently built on this work [35] to examine a simple model accounting for the heterogeneity of high explosives. They used the Mie-Grüneisen equation of state with energy release and added a passive scalar transport equation to model the explosive heterogeneity. The microstructures present in high explosives and conducive to hot-spots were simulated by a periodic variation in reaction rates associated with material elements. In this limited study, they were able to show that the average detonation front velocity was only modestly affected by the model heterogeneity. Their study was facilitated by the straightforward implementation of the equation of state that is described in the present paper.

Acknowledgements

This research was conducted at the Caltech ASCI ASAP Center of Excellence "Center for Simulation of Dynamic Response of Materials", contract B341492 under DOE Contract

W-7405-ENG-48. The authors would like to thank J. Quirk for the use of the Amrita computational facility.

References

[1] M.R. Baer and J. W. Nunziato. A 2-phase mixture theory for the deflagration-to-detonation transition (DDT) in reactive granular materials. *International Journal of Multiphase Flow*, 12(6):861–889, 1986.

[2] J.B. Bdzil, R. Menikoff, S.F. Son, A.K. Kapila, and D.S. Stewart. Two-phase modeling of deflagration-to-detonation transition in granular materials: A critical examination of modeling issues. *Phys. Fluids*, 11(2):378–402, 1999.

[3] D. Chakraborty, R.P. Muller, S. Dasgupta, and W.A. Goddard. The mechanism for unimolecular decomposition of RDX (1,3,5-trinitro-1,3,5-triazine), an ab initio study. *J. Phys. Chem. A*, 104(11):2261–2272, 2000.

[4] A. Chinnayya, E. Daniel, R. Saurel, G. Baudin, and C. Le Gallic. A new concept for the modeling of detonation waves in multiphase mixtures. In *12th Symp. (Intl) on Detonation*, pages 1–10, 2002.

[5] W. C. Davis. Equation of state for detonation products. In *10th Symp. (Intl) on Detonation*, pages 369–376, 1993.

[6] W. C. Davis. Complete equation of state for unreacted solid explosive. *Combustion and Flame*, 120 (3):399–403, 2000.

[7] B. M. Dobratz. LLNL Explosives Handbook - Properties of Chemical Explosives and Explosive Simulants. *LLNL Report UCRL-52997*, 1981.

[8] J. K. Dukowicz. A general, non-iterative Riemann solver for Godunov's method. *J. Comput. Phys.*, 61:119–137, 1985.

[9] Christopher A. Eckett. *Numerical and Analytical Studies of the Dynamics of Gaseous Detonations*. PhD thesis, California Institute of Technology, Pasadena, California, September 2000.

[10] R. P. Fedkiw, T. Aslam, B. Merriman, and S. Osher. A non-oscillatory Eulerian approach to interfaces in multimaterial flows (the Ghost Fluid Method). *J. Comput. Phys.*, 152:457–492, 1999.

[11] R. P. Fedkiw, A. Marquina, and B. Merriman. An isobaric fix for the overheating problem in multimaterial compressible flows. *J. Comput. Phys.*, 148:545–578, 1999.

[12] S. H. Fergason, A. Guardone, and B. M Argrow. Construction and validation of a dense gas shock tube. *J. Thermophys. and Heat Transfer*, 17(3):326–333, 2003.

[13] S. H. Fergason, T. L. Ho, B. M Argrow, and G. Emanuel. Theory for producing a single-phase rarefaction shock wave in a shock tube. *J. Fluid Mech.*, 445:37–54, 2001.

[14] W. Fickett and W. C. Davis. *Detonation*. University of California Press, 1979.

[15] J.E. Field, N.K. Bourne, S.J.P. Palmer, S.M. Walley, and J.M. Smallwood. Hot-spot ignition mechanisms for explosives and propellants. *Phil. Trans. R. Soc. Lond.* A, 339(1654):269–283, 1992.

[16] P. Glaister. An approximate linearised riemann solver for the euler equations for real gases. *J. Comput. Phys.*, 74:382–408, 1988.

[17] W. A. Goddard, D. I Meiron, M. Ortiz, and J. E. Shepherd. The 1998 center for simulation of dynamic response in meterials annual technical report. Technical Report cit-asci-tr032, California Institute of Technology, 1998.

[18] S. K. Godunov. A finite difference method for the computation of discontinuous solutions to the equations of fluid dynamics. *Mat. Sb.*, 47:271–306, 1959.

[19] K. A. Gonthier. *A Numerical Investigation of the Evolution of Self-Propagating Detonation Solids in Energetic Granular Solids*. PhD thesis, University of Notre Dame, 1996.

[20] K. A. Gonthier and J. M. Powers. A numerical investigation of transient detonation in granulated material. *Shock Waves*, 6:183–195, 1996.

[21] A. Harten. High resolution schemes for hyperbolic conservation laws. *J. Comput. Phys.*, 49:357–393, 1983.

[22] A. Harten, P. D. Lax, and B. van Leer. On upstream differencing and godunov type schemes for hyperbolic conservation laws. *SIAM Rev.*, 25:33–61, 1983.

[23] L. G. Hill. Detonation product equation-of-state directly from the cylinder test. In *21st Symp. (Intl) on Shock Waves*, 1997.

[24] J. N. Johnson, P. K. Tang, and C. A. Forest. Shock-wave initiation of heterogeneous reactive solids. *J. Appl. Phys.*, 57:4323–4334, 1985.

[25] R. J. Kee, F. M. Rupley, and James A. Miller. The CHEMKIN thermodynamic data base. Technical Report SAND87-8215, Sandia National Laboratories, 1987.

[26] J.W. Kury, R.D. Breithaupt, and C.M. Tarver. Detonation waves in trinitrotoluene. *Shock Waves*, 9(4):227–237, 1999.

[27] E. L. Lee and C. M. Tarver. Phenomenological model of shock initiation in heterogeneous explosives. *Phys. Fluids*, 23:2362–2372, 1980.

[28] M. S. Liou, B. van Leer, and J. S. Shen. Splitting of inviscid fluxes for real gases. *J. Comput. Phys.*, 87:1–24, 1990.

[29] C. L. Mader. *Numerical modeling of detonations*. University of California Press, 1979.

[30] C. L. Mader, J. D. Zumbro, and Eric N. Ferm. Proton radiographic and numerical modeling of colliding, diverging PBX-9502 detonations. In *12th Symp. (Intl) on Detonation*, pages 1–7, 2002.

[31] Jr Malcolm W. Chase, editor. *NIST-JANAF thermochemical tables*. Journal of Physical and Chemical Reference Data. American Chemical Society and American Institute of Physics for the National Institute of Standards and Technology, 4 edition, 1998. Monograph No. 9.

[32] S. P. Marsh. *LASL shock Hugoniot data*. University of California Press, 1980.

[33] S. McCahan and J. E. Shepherd. Thermodynamics of detonation products. In *10th Symp. (Intl) on Detonation*, pages 596–600, 1993.

[34] G. H. Miller and E. G. Puckett. A high-order Godunov method for multiple condensed phases. *J. Comput. Phys.*, 128:134–164, 1996.

[35] E. O. Morano and J. E. Shepherd. Effect of reaction rate periodicity on detonation propagation. In *Shock Compression of Condensed Matter*, pages 446–449, 2001.

[36] E. S. Oran and J. P. Boris. *Numerical Simulation of Reactive Flow*. Prentice Hall, 1987.

[37] E. S. Oran and J. P. Boris. Studies of detonation initiation, propagation, and quenching. In Elaine S. Oran and Jay P. Boris, editors, *Numerical Approaches to Combustion Modeling*, volume 135 of *Prog. Astronaut. Aeronaut.* AIAA, Washington DC, 1991.

[38] Elaine S. Oran, James W. Weber, Jr., Eliza I. Stefaniw, Michel H. Lefebvre, and John D. Anderson, Jr. A numerical study of a two-dimensional H_2–O_2–Ar detonation using a detailed chemical reaction model. *Combust. Flame*, 113:147–163, 1998.

[39] G. Paczko and R. Klein. Reduced chemical kinetic schemes for hydrogen–air–steam detonation simulations. Unpublished. Presented at *14th ICDERS*, Coimbra, Portugal, 1993.

[40] K. Prasad, R.A. Yetter, and M.D. Smooke. An eigenvalue method for computing the burning rates of RDX propellants. *Combust. Sci. Technol.*, 124(1-6):35–82, 1997.

[41] W. H. Press, S. A. Teukolsky, W. T. Vetterling, and B. P. Flannery. *Numerical Recipes in Fortarn 77, the art of scientific computing, second edition*. Cambridge University Press, 1992.

[42] J. J. Quirk. AMRITA - A computational facility (for CFD modelling). In *VKI 29th Lecture Series*, 1998.

[43] P. L. Roe. Approximate Riemann solvers, parameter vectors and difference schemes. *J. Comput. Phys.*, 43:357–372, 1981.

[44] R. Sanders, E. Morano, and M. C. Druguet. Multidimensional dissipation for upwind schemes: Stability and applications to gas dynamics. *J. Comput. Phys.*, 145:511–537, 1998.

[45] R. Saurel and S. Massoni. On Riemann-problem-based methods for detonations in solid energetic materials. *International Journal for Numerical Methods in Fluids*, 26:101–121, 1998.

[46] J. S. Shen, M. S. Liou, and B. van Leer. Inviscid flux-splitting algorithms for real gases with non-equilibrium chemistry. *J. Comput. Phys.*, 90:371–395, 1990.

[47] C. W. Shu and S. Osher. Efficient implementation of essentially non-oscillatory shock-capturing schemes. *J. Comput. Phys.*, 77:439–471, 1988.

[48] A. Soria and F. Casadei. Arbitrary Lagrangian-Eulerian multicomponent compressible flow with fluid-structure interaction. *International Journal for Numerical Methods in Fluids*, 25:1263–1284, 1997.

[49] D. S. Stewart, J. Yao, and W. C. Davis. Computation of shock acceleration effects on detonation shock dynamics for explosives described by general equation of state. *Proc. of the Combust. Inst.*, 28:619–628, 2000.

[50] D. S. Stewart, Sunhee Yoo, and W. C. Davis. Equation of state for modeling the detonation reaction zone. In *12th Symp. (Intl) on Detonation*, pages 1–11, 2002.

[51] G. Strang. On the construction and comparison of difference schemes. *SIAM Journal on Numerical Analysis*, 5 (3):506–517, 1968.

[52] T. Tang. Convergence analysis for operator-splitting methods applied to conseervation laws with stiff source terms. *SIAM J. Numer. Anal.*, 35:1939–1968, 1998.

[53] J. C. Tannehill, D. A. Anderson, and R. H. Pletcher. *Computational fluid mechanics and heat transfer*. Taylor & Francis, 1997.

[54] P. A. Thompson. *Compressible fluid dynamics*. McGraw-Hill Book Company, 1972.

[55] P. A. Thompson, G. C. Carofano, and Y. Kim. Shock waves and phase changes in a large-heat-capacity fluid emerging from a tube. *J. Fluid Mech.*, 166:57–92, 1986.

[56] E. F. Toro, M. Spruce, and W. Spearce. Restoration of the contact surface in the HLL-type Riemann solver. *Shock Waves*, 4:25–34, 1994.

[57] B. van Leer. Flux-vector splitting for the Euler equations. *Lecture Notes in Physics*, 170:507–512, 1982.

[58] P. Vitello and P. C. Souers. Stability effects of artificial viscosity in detonation modeling. In *12th Symp. (Intl) on Detonation*, pages 1–8, 2002.

[59] Jr. W.C. Gardiner, editor. *Gas-phase combustion chemistry*. Springer, New York, 2000.

[60] S. Xu and D. S. Stewart. Deflagration-to-detonation transition in porous energetic materials: A comparative model study. *Journal of Engineering Mathematics*, 31:143–172, 1997.

[61] Ya. B. Zel'dovich and Yu. P. Raizer. *Physics of shock waves and high-temperature hydrodynamic phenomena*, volume II. Academic Press, 1966.

[62] V. N. Zharkov and V. A. Kalinin. *Equations of state for solids at high pressures and temperatures*. Consultants Bureau, New-York, 1971.

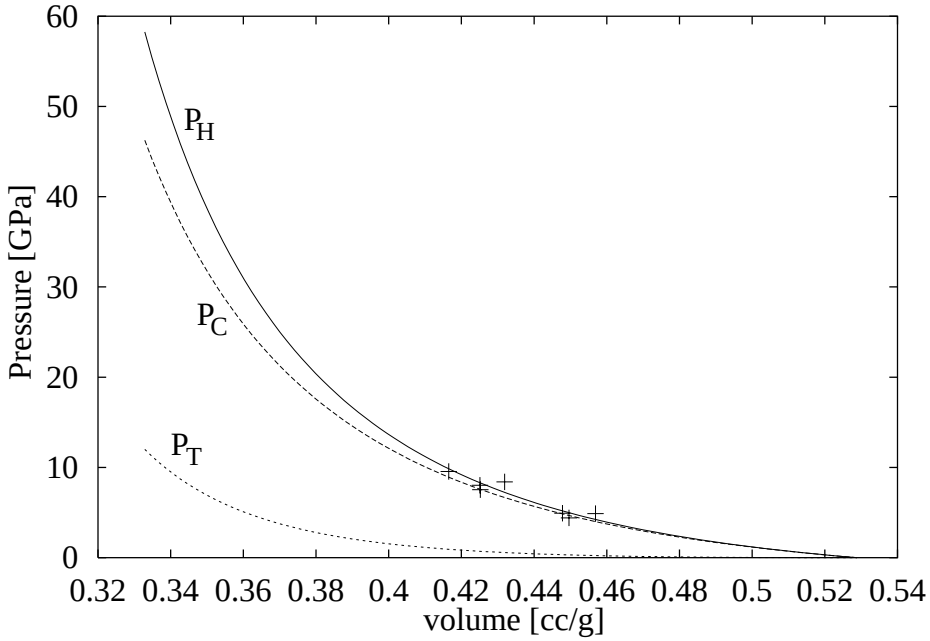

Figure 1: HMX Hugoniot pressure ($P_{\mathcal{H}}$), cold component (P_C), thermal component (P_T), and shock-compression data (+) from [32].

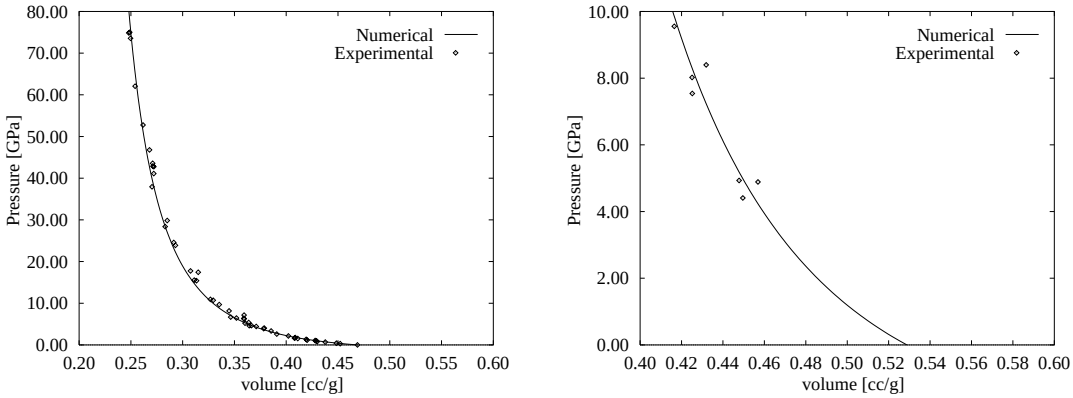

(a) (b)

Figure 2: Hugoniot pressure $P_{\mathcal{H}}(v)$ from (7) and experimental data from [32]. (a) Kel-F $\mathcal{G} = 0.45$. (b) HMX_sp $\mathcal{G} = 0.7$.

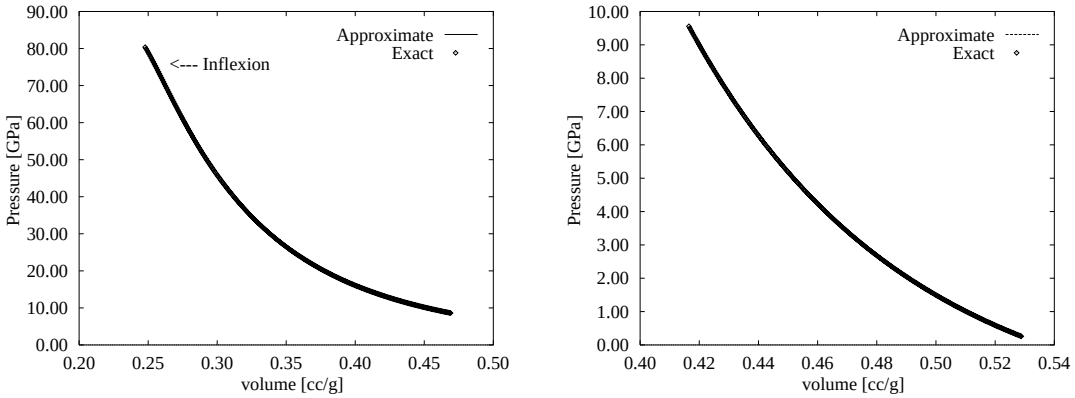

(a) (b)

Figure 3: Verification of the numerical computation of $P_s(v)$, the isentropic pressure, (a) Kel-F $\mathcal{G} = 2$ (b) HMX_sp $\mathcal{G} = 2$.

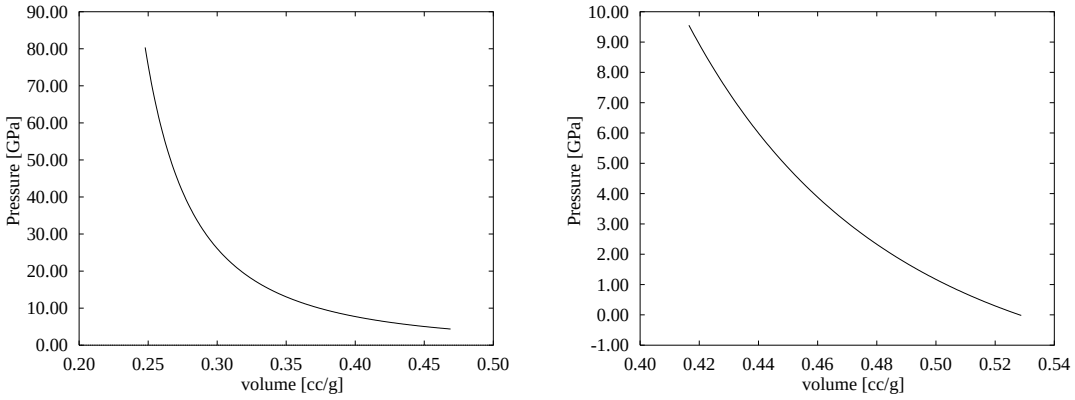

(a) (b)

Figure 4: Isentropic pressure $P_s(v)$ using tablee 3, (a) Kel-F $\mathcal{G} = 0.45$ (b) HMX_sp $\mathcal{G} = 0.7$.

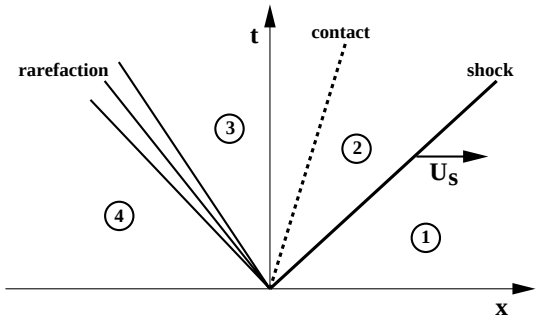

Figure 5: Wave system and states created by "shock tube" initial conditions.

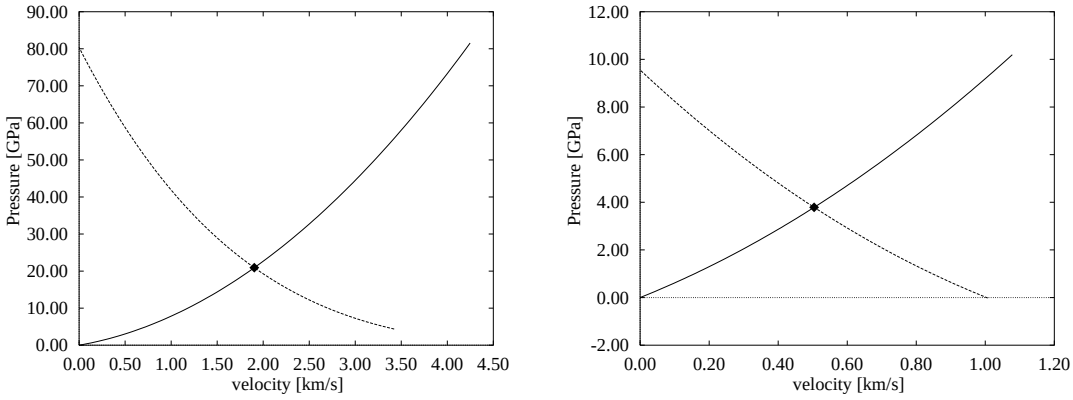

(a) (b)

Figure 6: Pressure vs. velocity at $t = 0.02\,\mu$s, (a) Kel-F $\mathcal{G} = 0.45$ (b) HMX_sp $\mathcal{G} = 0.70$.

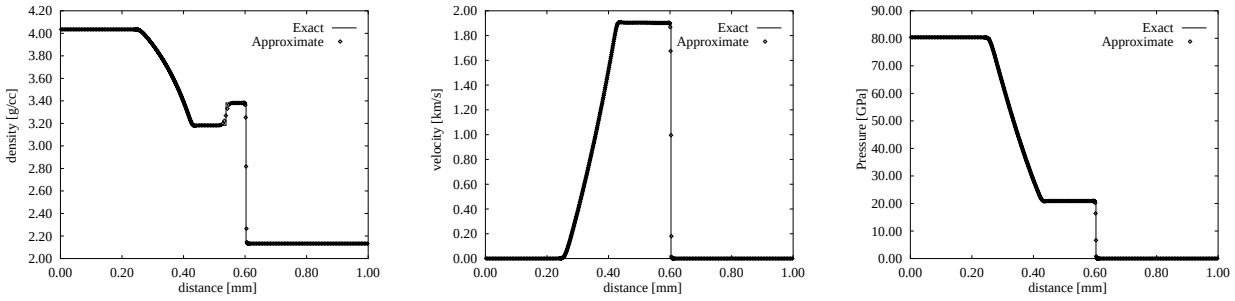

(a) (b) (c)

Figure 7: Kel-F inert shock tube experiment at $t = 0.02\,\mu$s.

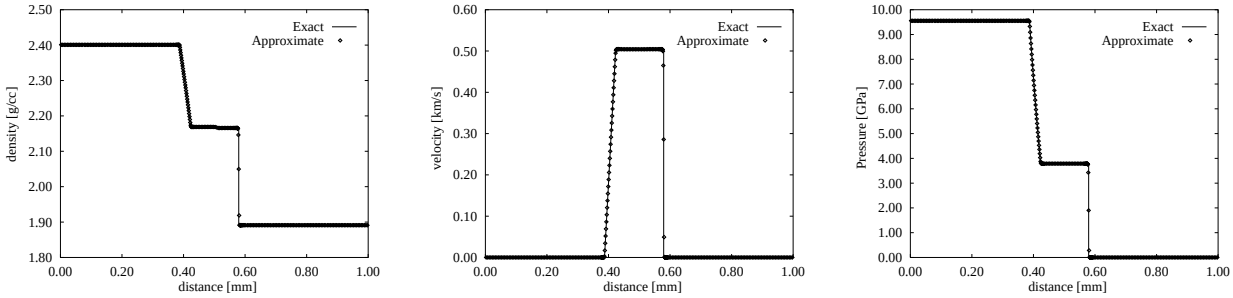

(a) (b) (c)

Figure 8: HMX_sp inert shock tube experiment at $t = 0.02\,\mu$s.

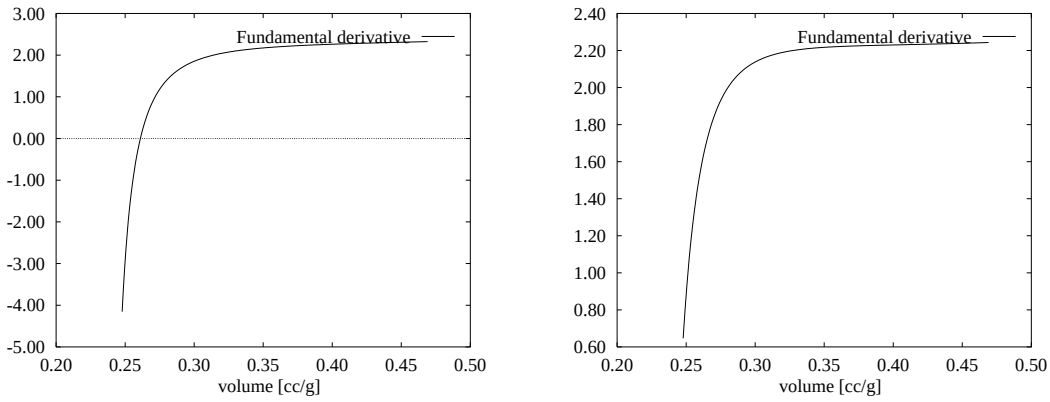

(a) (b)

Figure 9: Fundamental derivative Γ vs. v (a) Kel-F $\mathcal{G} = 2$ (b) Kel-F $\mathcal{G} = 1.7$

.

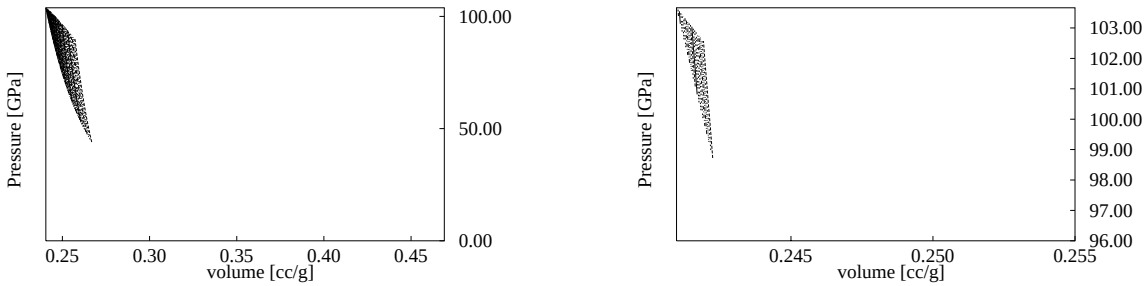

(a) (b)

Figure 10: Isocontours of negative Γ in the (P, v) plane. (a) Kel-F ($\mathcal{G} = 2$) (b) Kel-F ($\mathcal{G} = 1.7$)

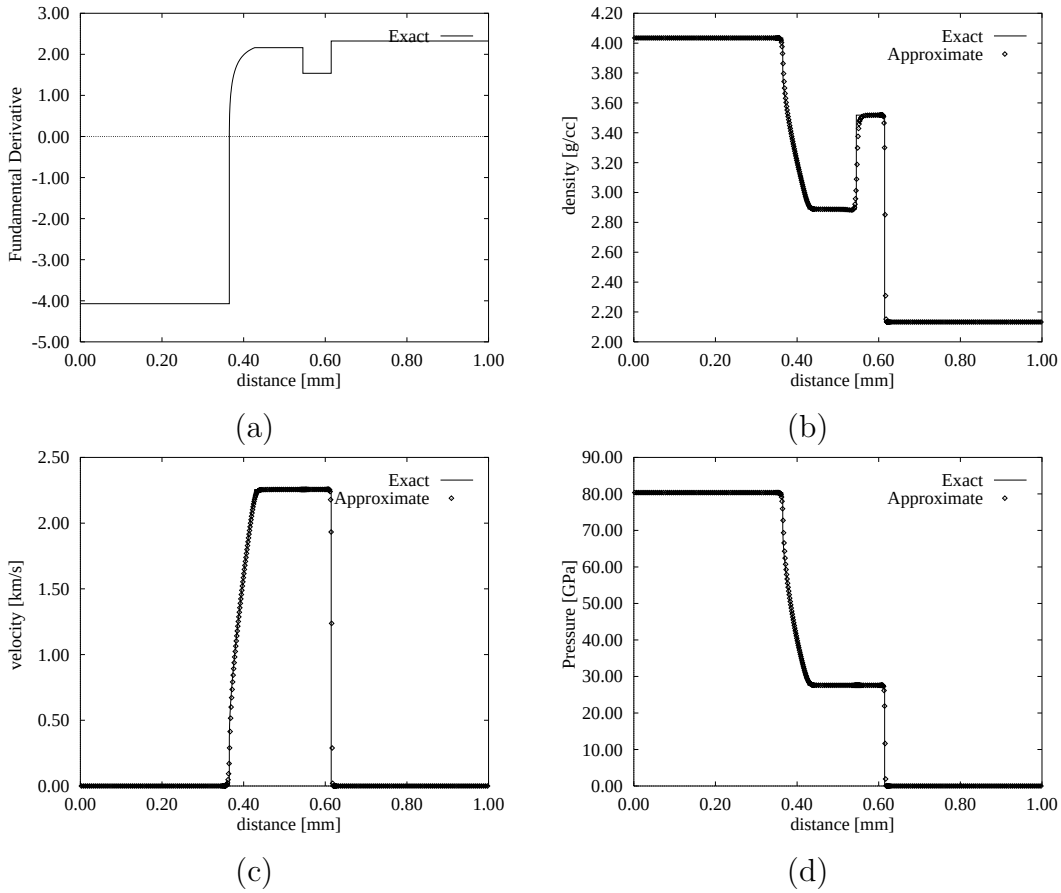

Figure 11: Kel-F inert shock tube experiment at $t = 0.02\,\mu$s.

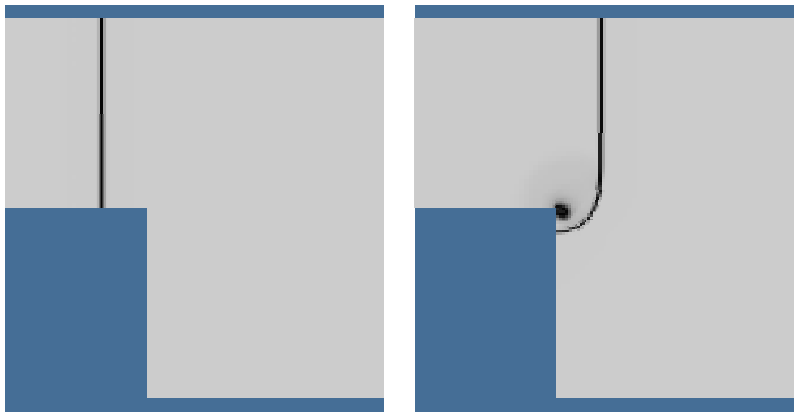

(a) (b)

Figure 12: Inert HMX_sp shock-diffraction (a) $t = 1.56$ μs (b) $t = 3.55$ μs.

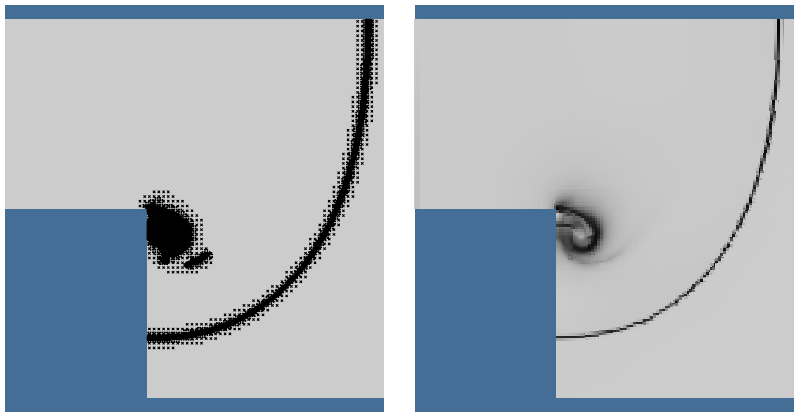

(a) (b)

Figure 13: Inert HMX_sp shock diffraction at $t = 7.49$ μs: (a) computational cells flagged for refinement; (b) numerical Schlieren.

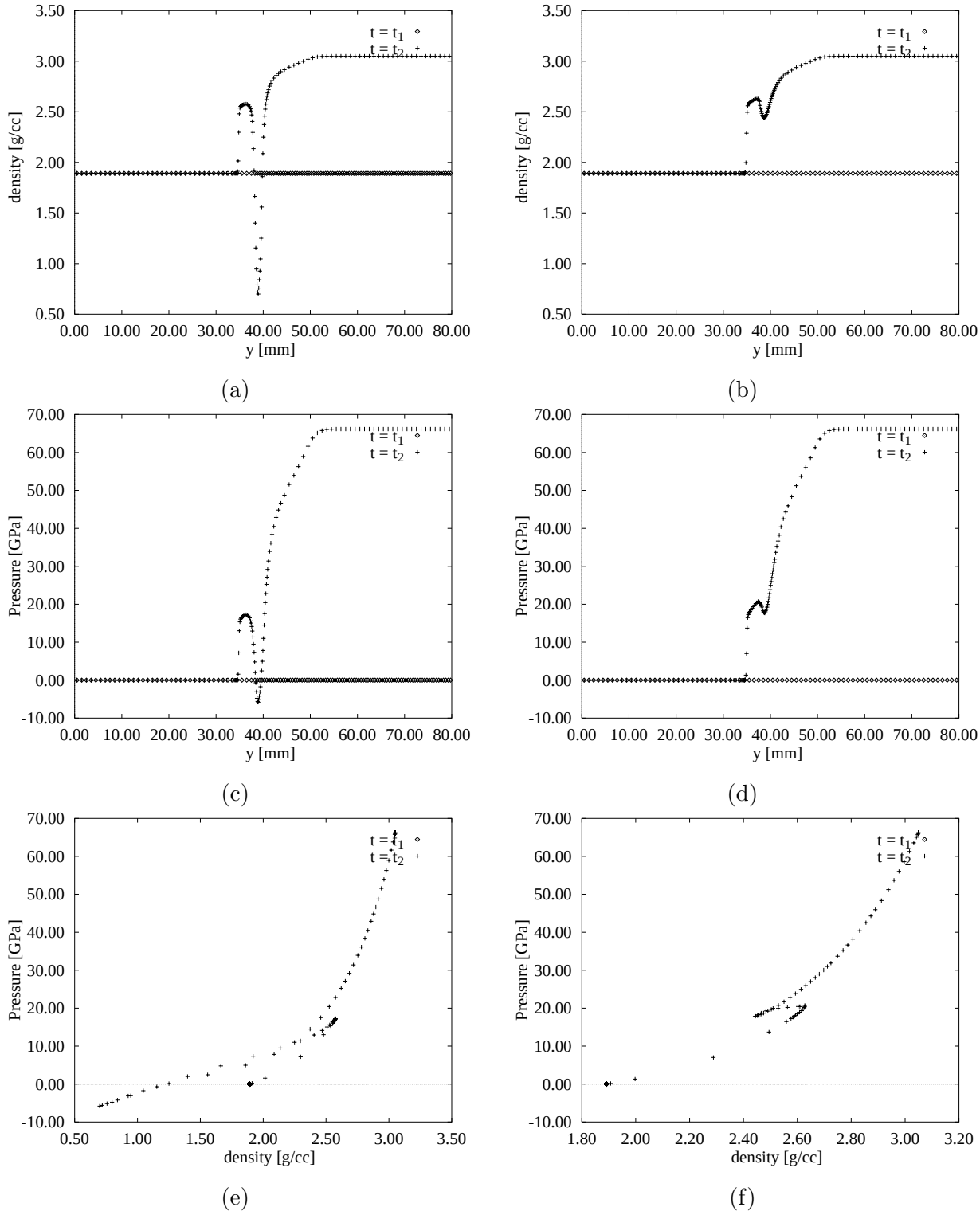

Figure 14: Cross-sections of the solution for HMX_sp inert shock diffraction at $t_1 = 1.56$ μs (reference state, indicated by $\diamond$) and at $t_2 = 3.55$ μs (+) at $x = 31$ mm (left column) and at $x = 32$ mm (right column).

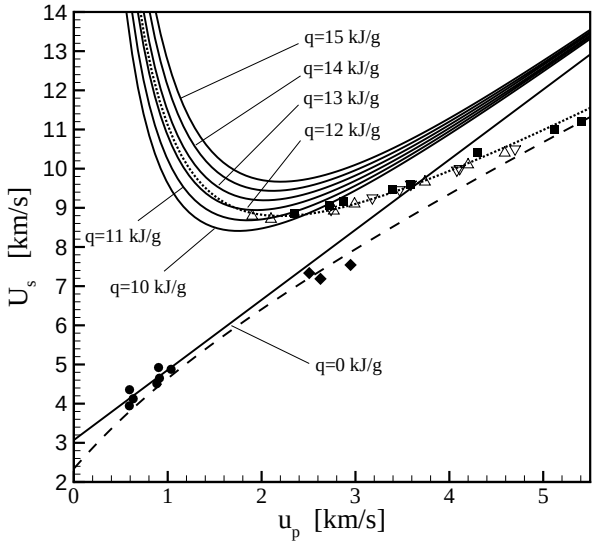

Figure 15: U_s–u_p diagram (——) parametrized by the energy release q for the Mie-Grüneisen HMX model according to equation (38). The values of c_0, s and $\mathcal{G}$ are listed in table 3. Also shown is the U_s–u_p diagram derived by Stewart et al. [50] for the HMX-based explosives PBX 9404-9501 for reactants (– – –) and products (· · · · · ·). The symbols are shock compression data for single-crystal (⧫) and solvent-pressed HMX (●) [32], as well as detonation data reported in [50] for PBX 9404-9501.

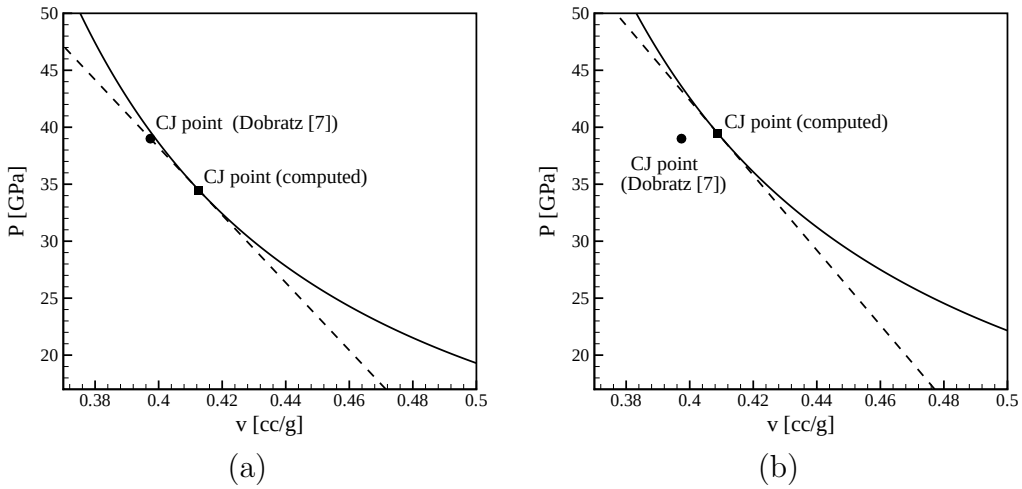

Figure 16: Product Hugoniot curve (——) and Rayleigh line (– – –) for HMX_sp: (a) computed with $q = 12.67\,\mathrm{kJ/g}$ and $U_s = 9.11\,\mathrm{km/s}$; (b) computed with $q = 14.67\,\mathrm{kJ/g}$ and $U_s = 9.60\,\mathrm{km/s}$. The square is the computed CJ point, the circle is the experimental value from [7].

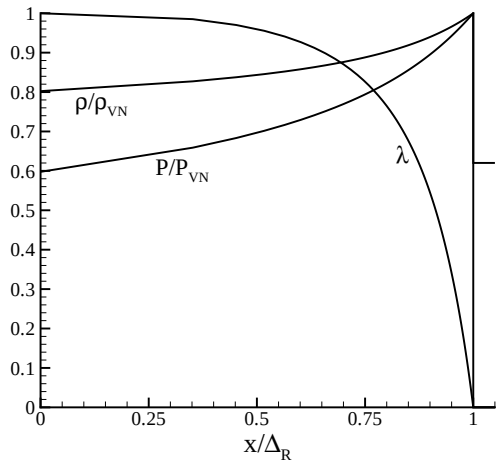

Figure 17: ZND profile of density, mass fraction and pressure as a function of distance normalized by the total length of the reaction zone, Δ_R. Pressure and density are normalized by their respective post-shock, or von Neumann, values. Particle velocity is proportional to P in the limit of a strong shock, and it is not shown here.

.

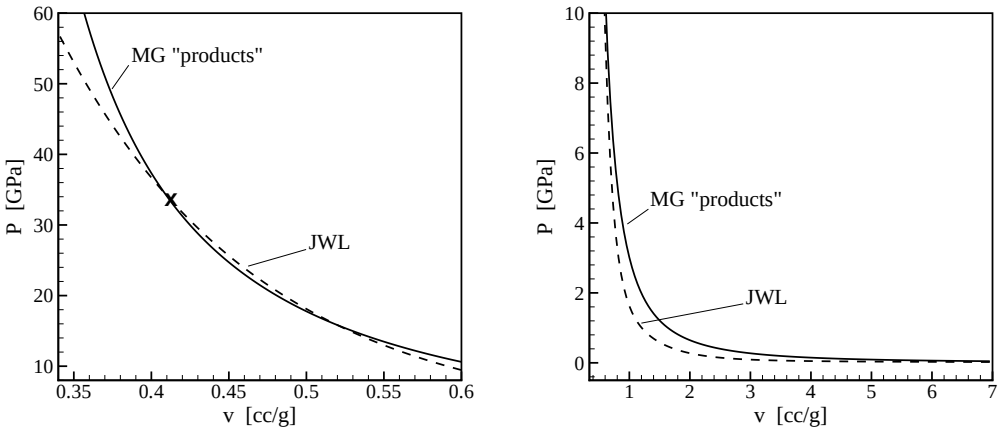

Figure 18: Mie-Grüneisen product isentrope (——) with $q = 14.67\,\mathrm{kJ/g}$, $U_s = 9.60\,\mathrm{km/s}$ and HMX data from table 3; JWL isentrope (– – –) from table 7. The two curves are centered at the state marked by **x** in frame (a), at $v_i = 0.43\,\mathrm{cc/g}$. In (a) the pressure range is 10–60 GPa; in (b) the pressure range is 0–10 GPa.

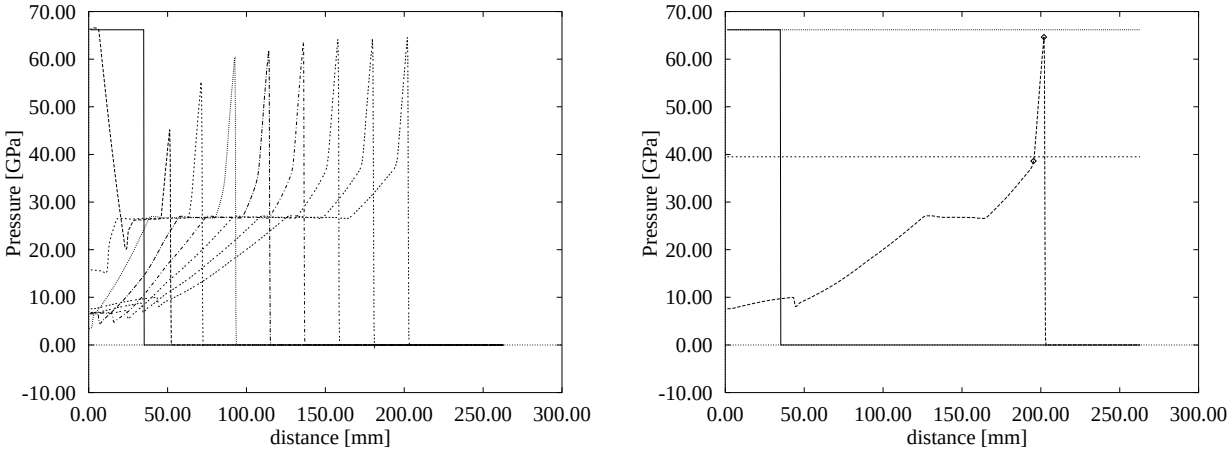

(a) (b)

Figure 19: Detonating HMX shock tube experiment for $q = 14.67\,\mathrm{kJ/g}$. Frame (a) shows a sequence of pressure diagrams as a function of distance plotted at regular time intervals. Frame (b) shows the initial conditions (——) and the final solution (– – –). Also indicated are the expected CJ pressure, $P_{CJ,\,calc} = 39.51$ GPa, and VN pressure, $P_{VN,\,calc} = 66.17$ GPa.

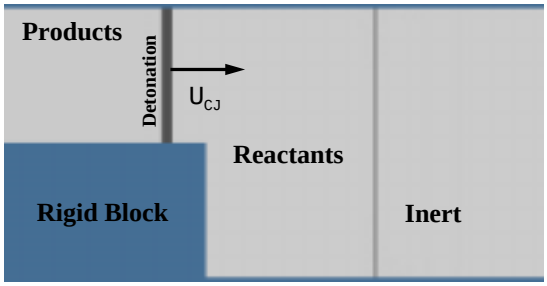

Figure 20: Geometry for shock diffraction simulation.

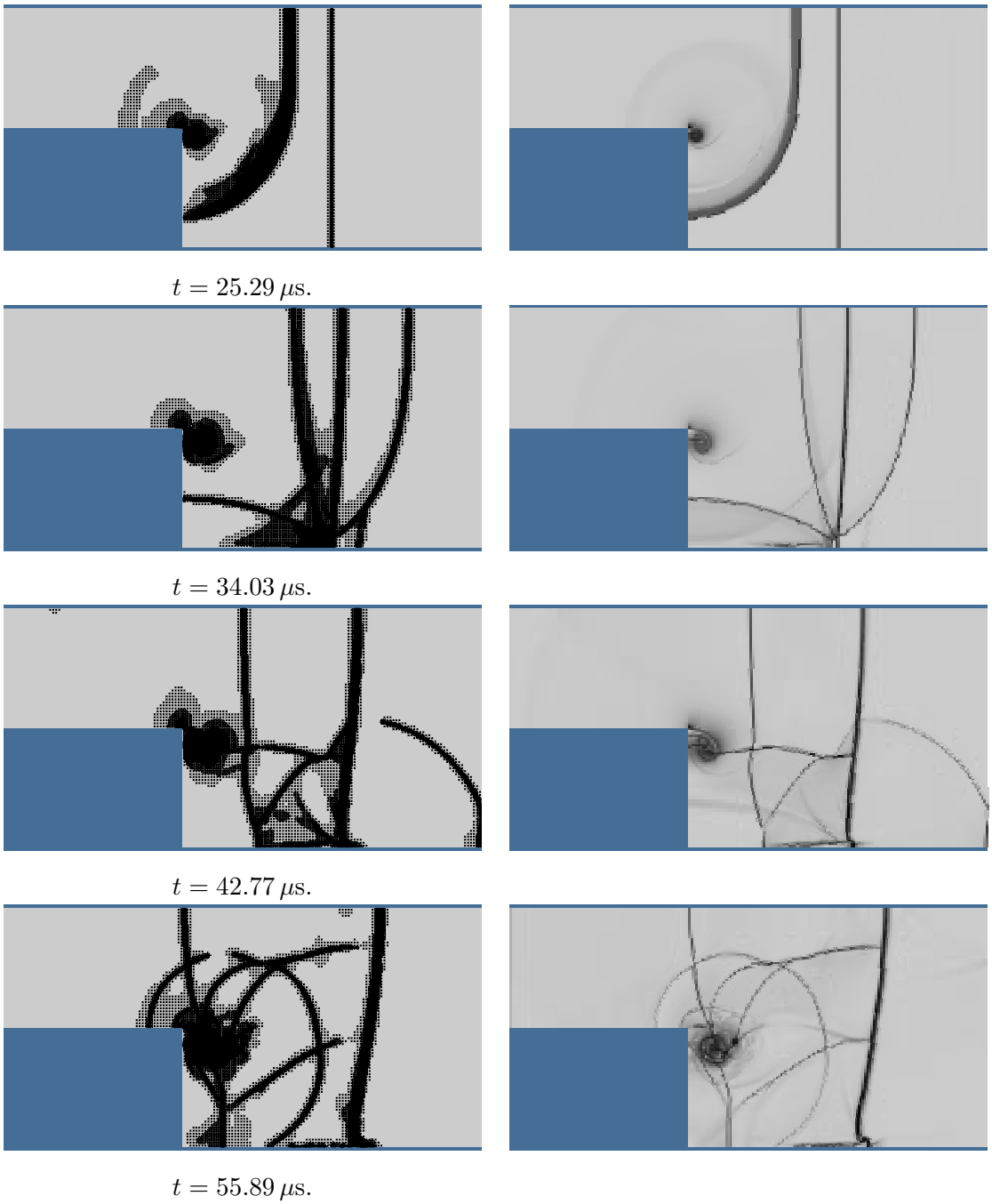

Figure 21: Detonation diffraction example with a pressure-independent rate ($\nu = 0$): (a) refinement flags; (b) Schlieren images.

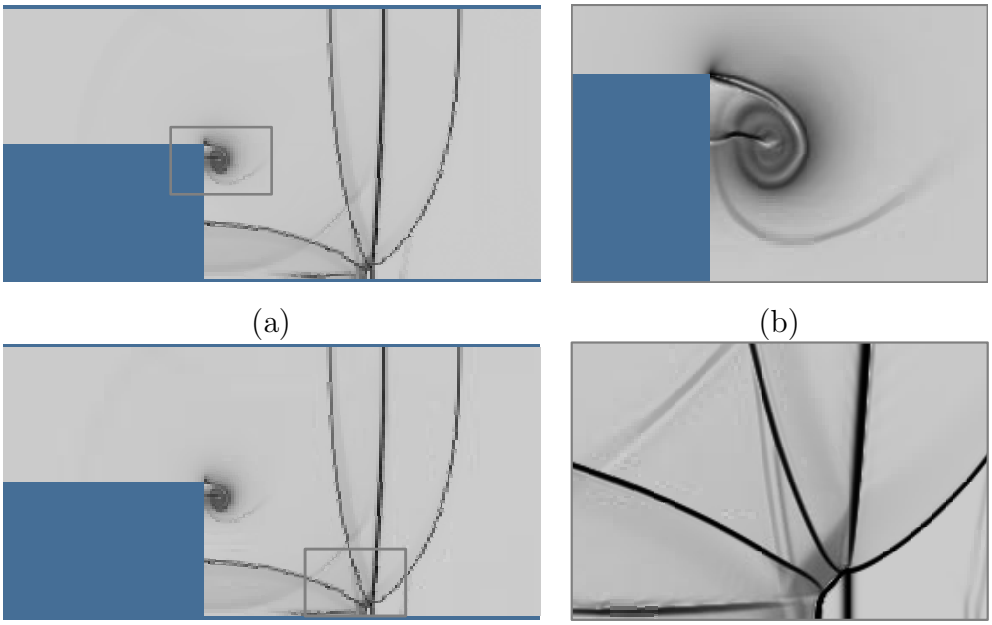

Figure 22: Details of selected flow features at $t = 34.03\,\mu$s: (a), (b) corner vortex; (c), (d) shock interaction at lower boundary.

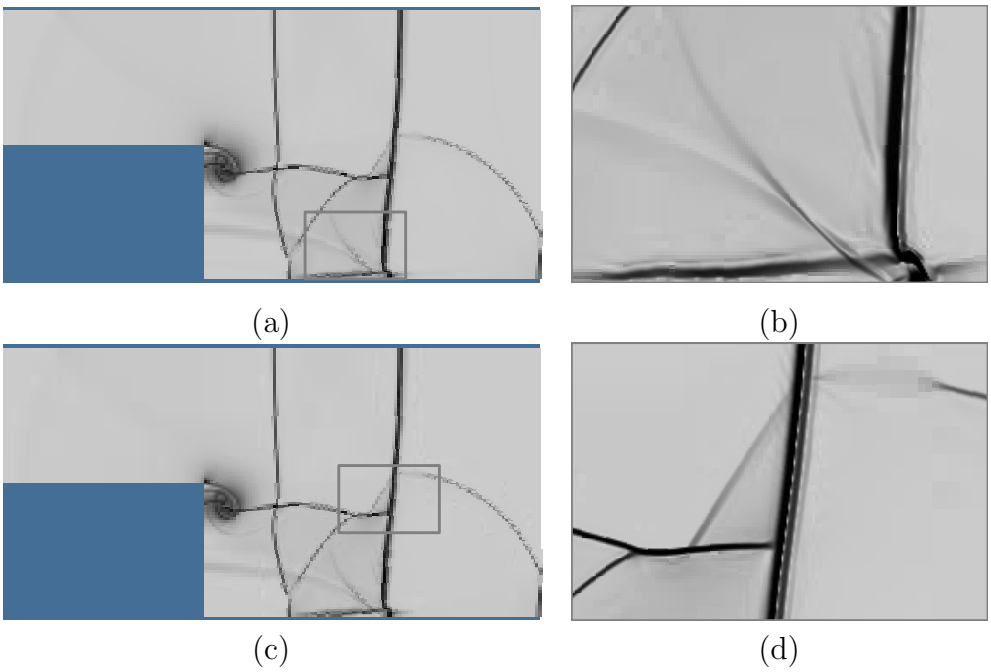

Figure 23: Details of selected flow features $t = 42.77\,\mu$s. (a), (b) contact surface; (c), (d) reflected shock interaction with contact surface showing precursor wave on slow-fast type interface.

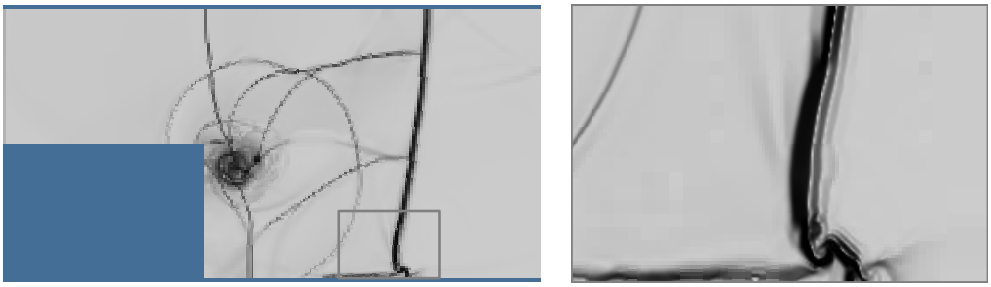

(a) (b)

Figure 24: Close-up of instability of contact surface at $t = 55.89\,\mu$s.

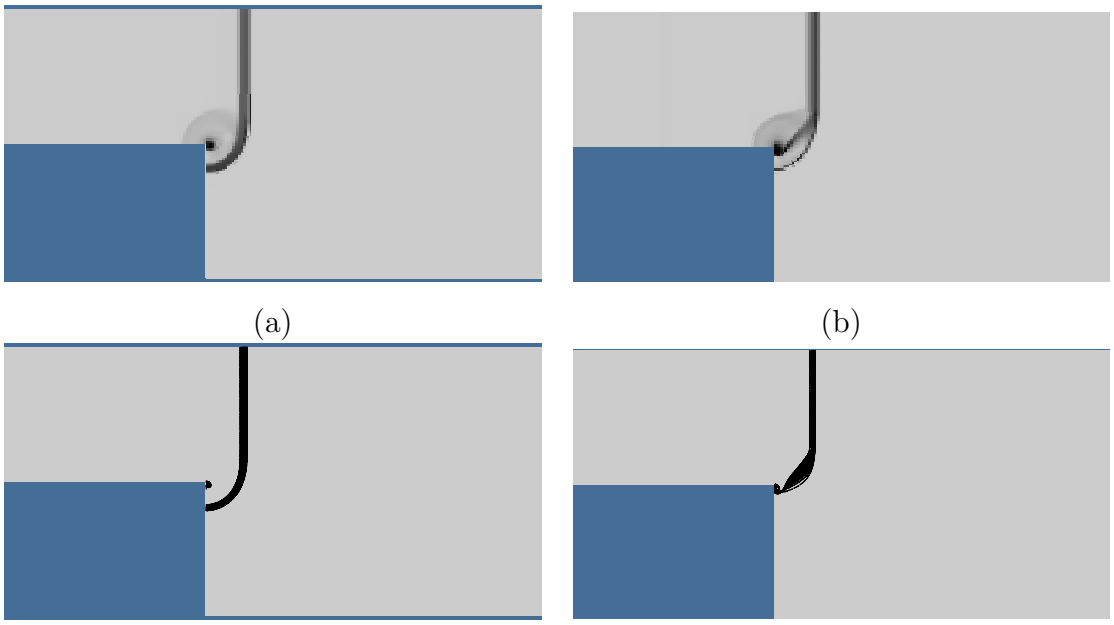

Figure 25: Comparison of detonation diffraction calculated with pressure-independent reaction rate ($\nu = 0$), frames (a) and (c); and pressure-dependent reaction rate ($\nu = 5$), frames (b) and (d). Top row contains Schlieren images and bottom row contains mass fraction contours. The incident wave has moved downstream a distance that is approximately 44% of the total traveled distance in this calculation.

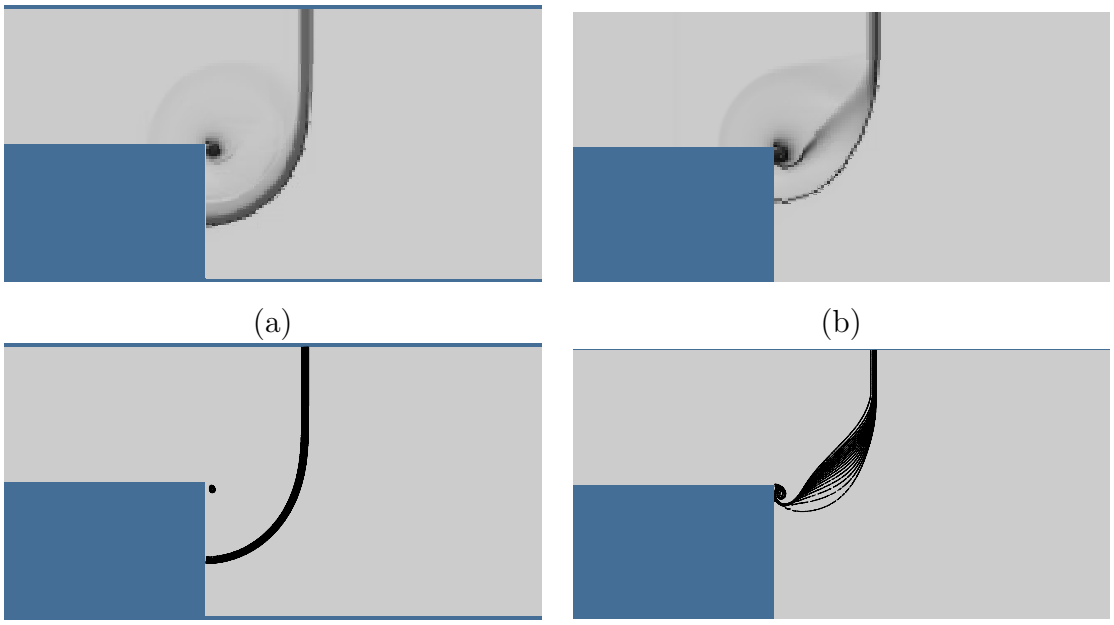

Figure 26: Comparison of detonation diffraction calculated with pressure-independent reaction rate ($\nu = 0$), frames (a) and (c); and pressure-dependent reaction rate ($\nu = 5$), frames (b) and (d). Top row contains Schlieren images and bottom row contains mass fraction contours. The incident wave has moved downstream a distance that is approximately 56% of the total traveled distance in this calculation.

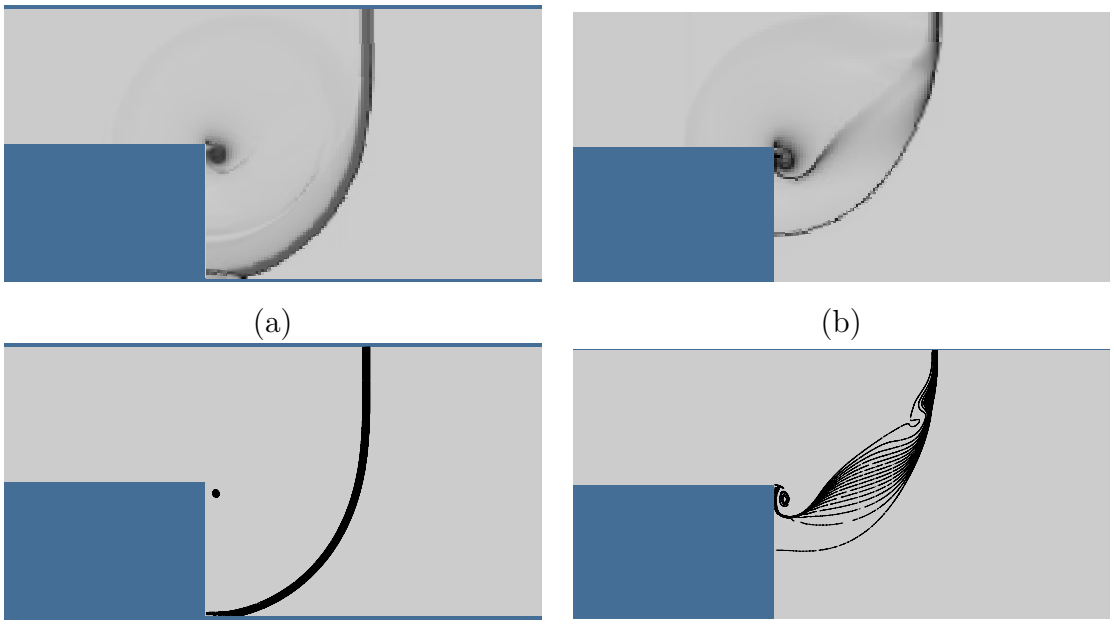

Figure 27: Comparison of detonation diffraction calculated with pressure-independent reaction rate ($\nu = 0$), frames (a) and (c); and pressure-dependent reaction rate ($\nu = 5$), frames (b) and (d). Top row contains Schlieren images and bottom row contains mass fraction contours. The incident wave has moved downstream a distance that is approximately 69% of the total traveled distance in this calculation.